PAPER • OPEN ACCESS

Enhanced total variation minimization for stable image reconstruction

To cite this article: Congpei An *et al* 2023 *Inverse Problems* **39** 075005

You may also like

Enhanced total variation minimization for stable image reconstruction

Congpei An[1], Hao-Ning Wu[2] and Xiaoming Yuan[2,*]

[1] School of Mathematics, Southwestern University of Finance and Economics, Chengdu, People's Republic of China
[2] Department of Mathematics, The University of Hong Kong, Hong Kong, People's Republic of China

E-mail: xmyuan@hku.hk

Abstract

The total variation (TV) regularization has phenomenally boosted various variational models for image processing tasks. We propose to combine the backward diffusion process in the earlier literature on image enhancement with the TV regularization, and show that the resulting enhanced TV minimization model is particularly effective for reducing the loss of contrast. The main purpose of this paper is to establish stable reconstruction guarantees for the enhanced TV model from noisy subsampled measurements with two sampling strategies, non-adaptive sampling for general linear measurements and variable-density sampling for Fourier measurements. In particular, under some weaker restricted isometry property conditions, the enhanced TV minimization model is shown to have tighter reconstruction error bounds than various TV-based models for the scenario where the level of noise is significant and the amount of measurements is limited. The advantages of the enhanced TV model are also numerically validated by preliminary experiments on the reconstruction of some synthetic, natural, and medical images.

Keywords: total variation, image reconstruction, backward diffusion, anisotropic, loss of contrast, stability, difference-of-convex regularization

(Some figures may appear in colour only in the online journal)

---

* Author to whom any correspondence should be addressed.

1. Introduction

Since the work of Rudin *et al* [55], various variational models based on the total variation (TV) have been intensively studied for image processing problems; see, e.g. [15, 17] for reviews. Given linear measurements $y \in \mathbb{C}^m$ observed via

$$y = \mathcal{M}\bar{X} + e \tag{1.1}$$

from an unknown image $\bar{X} \in \mathbb{C}^{N \times N}$, where $\mathcal{M} : \mathbb{C}^{N \times N} \to \mathbb{C}^m$ is a linear operator defined component-wisely by

$$[\mathcal{M}(\bar{X})]_j := \langle M_j, \bar{X} \rangle = \mathrm{tr}(M_j \bar{X}^*),$$

for suitable matrices M_j with m considerably smaller than N^2, and $e \in \mathbb{C}^m$ is a noise term bounded by $\|e\|_2 \leqslant \tau$ with level $\tau \geqslant 0$, reconstruction of the unknown $\bar{X}$ can be modeled as the following TV minimization problem:

$$\min_{X \in \mathbb{C}^{N \times N}} \|X\|_{\mathrm{TV}} \quad \text{s.t.} \quad \|\mathcal{M}X - y\|_2 \leqslant \tau, \tag{1.2}$$

where $\|\cdot\|_{\mathrm{TV}}$ is the TV semi-norm. Note that the TV semi-norm can be mainly categorized as the isotropic [13] and anisotropic [14] cases for discrete images. In this paper, we discuss how to enhance the canonical constrained TV model (1.2) by the recently proposed springback regularization in [4] for image reconstruction and establish stable reconstruction guarantees.

As profoundly analyzed in [47], the constrained TV model (1.2) has the advantage of reconstructing high-quality images from a relatively small number of measurements. Theoretical analysis in [47] is mainly based on the seminal compressed sensing (CS) works [10, 23]. Note that the classic CS theory assumes the sparsity of the (vector) signal of interest or its coefficients under certain transformations. Correspondingly the signal reconstruction can be modeled as some ℓ_1-norm minimization problems. The CS theory can be extended to image reconstruction because natural images usually have (approximately) sparse gradients. Indeed, mathematically the TV semi-norm of a discrete image $X \in \mathbb{C}^{N \times N}$ is just the sum of the magnitudes of all entries $|[\nabla X]_{j,k}|$ in its gradient $\nabla X \in \mathbb{C}^{N \times N \times 2}$. That is,

$$\|X\|_{\mathrm{TV}} := \|\nabla X\|_1 = \sum_{j,k} |[\nabla X]_{j,k}|, \tag{1.3}$$

where the definitions of ∇X and $|[\nabla X]_{j,k}|$ are given as follows. For any image $X \in \mathbb{C}^{N \times N}$ represented by an $N \times N$ block of pixel intensities with all intensities $X_{j,k}$ in $[0,1]$, the discrete directional derivatives of $X \in \mathbb{C}^{N \times N}$ are defined in a pixel-wise manner as

$$X_x : \mathbb{C}^{N \times N} \to \mathbb{C}^{(N-1) \times N}, \quad (X_x)_{j,k} := X_{j+1,k} - X_{j,k},$$
$$X_y : \mathbb{C}^{N \times N} \to \mathbb{C}^{N \times (N-1)}, \quad (X_y)_{j,k} := X_{j,k+1} - X_{j,k}.$$

The discrete gradient transform $\nabla : \mathbb{C}^{N \times N} \to \mathbb{C}^{N \times N \times 2}$ is defined in a matrix form as

$$[\nabla X]_{j,k} := \begin{cases} ((X_x)_{j,k}, (X_y)_{j,k}), & 1 \leqslant j \leqslant N-1,\ 1 \leqslant k \leqslant N-1, \\ (0, (X_y)_{j,k}), & j = N,\ 1 \leqslant k \leqslant N-1, \\ ((X_x)_{j,k}, 0), & 1 \leqslant j \leqslant N-1,\ k = N, \\ (0, 0), & j = k = N. \end{cases}$$

If the magnitude $|[\nabla X]_{j,k}|$ is defined as $|(X_x)_{j,k}| + |(X_y)_{j,k}|$, then it leads to the *anisotropic TV semi-norm* $\|\cdot\|_{\mathrm{TV}_a}$ as defined in [14, 24], that is, the sum of the magnitudes of its discrete gradient

$$\|X\|_{\mathrm{TV}_a} := \sum_{j,k} |(X_x)_{j,k}| + |(X_y)_{j,k}|. \tag{1.4}$$

If $|[\nabla X]_{j,k}|$ is defined as $\sqrt{(X_x)_{j,k}^2 + (X_y)_{j,k}^2}$, then it leads to the *isotropic TV semi-norm* $\|\cdot\|_{\mathrm{TV}_i}$ as defined in [13]:

$$\|X\|_{\mathrm{TV}_i} := \sum_{j,k} \sqrt{(X_x)_{j,k}^2 + (X_y)_{j,k}^2}.$$

If we regard ∇X as an $N^2 \times 2$ matrix, then $\|X\|_{\mathrm{TV}_a}$ and $\|X\|_{\mathrm{TV}_i}$ are the $\ell_{1,1}$ and $\ell_{2,1}$ norms of ∇X, respectively. Since both TV semi-norms are equivalent subject to a factor of $\sqrt{2}$ in the sense that

$$\|X\|_{\mathrm{TV}_i} \leqslant \|X\|_{\mathrm{TV}_a} \leqslant \sqrt{2}\|X\|_{\mathrm{TV}_i}, \tag{1.5}$$

similarly to [47], we only consider the anisotropic case for succinctness and the following discussion can be extended to the isotropic case analogously. Moreover, note that $\|\nabla X\|_2 = (\sum_{j,k}(X_x)_{j,k}^2 + (X_y)_{j,k}^2)^{1/2}$ in the second component of the enhanced TV regularization (1.6) is the $\ell_{2,2}$ norm of ∇X.

Models using the ℓ_1-norm are fundamental to various CS problems, while solutions to such models may be over-penalized because the ℓ_1 regularization tends to underestimate the high-amplitude components of the solution, as analyzed in [25]. Accordingly, many non-convex alternatives have been proposed in the literature to overcome this pitfall and thus promote sparsity more firmly; see, e.g. the ℓ_p $(0 < p < 1)$ regularization [21, 27], the ℓ_{1-2} regularization [6, 29, 38, 42, 67–69], and the transformed ℓ_1 regularization [72, 73]. The non-convexity feature in image processing has also been emphasized in various papers; see, e.g. [48]. Recently, we proposed the springback regularization in [4], and it can be generalized as the following for discrete images:

$$\mathcal{R}_\alpha(X) := \|\nabla X\|_1 - \frac{\alpha}{2}\|\nabla X\|_2^2, \tag{1.6}$$

where $\alpha > 0$ is a meticulously-chosen parameter to ensure the positiveness or the well-definedness of (1.6), $\|\nabla X\|_1$ is the TV term (1.3) and we focus on the anisotropic definition (1.4) in this paper, and $\|\nabla X\|_2^2$ is the sum of the squared magnitudes of ∇X. Note that the springback regularization (1.6) is of difference-of-convex. To some extent, it keeps both the nice recoverability of various non-convex surrogates of the TV regularization and the computability of the original TV regularization. To be consistent with the TV literature, we call (1.6) an *enhanced TV* regularization in this paper.

Non-convex penalties proposed in the CS literature are mainly rooted in the field of statistics, and they are usually applied in straightforward ways in the image processing literature. Interestingly, as elaborated in section 1.1, the enhanced TV regularization (1.6) has some intrinsic interpretations from the perspective of image processing. We are thus encouraged to consider the enhanced TV model

$$\min_{X \in \mathbb{C}^{N \times N}} \mathcal{R}_\alpha(X) \quad \text{s.t.} \quad \|\mathcal{M}X - y\|_2 \leqslant \tau \tag{1.7}$$

for image reconstruction, and we aim at establishing some stable reconstruction guarantees theoretically. It is worth noting that, despite the theoretical reconstruction guarantees established in [4] for sparse signals or signals that are sparse after an orthonormal transform, the guarantees established in [4] are not applicable to the enhanced TV model (1.7). The reason is

that the gradient transform $\nabla : X \to \nabla X$ fails to be orthonormal, as mentioned in [47]. Also, we notice that the idea of enhancing the TV regularization (the isotropic version) with a subtraction of a squared norm of the image gradient was skated over in [45], and it was empirically tested for some image denoising problems despite the lack of rigorous study for reconstruction guarantees from a few measurements.

1.1. An image processing view of the enhanced TV regularization

Solutions to TV-based models may lose contrast across edges. That is, the contrast of the regions on both sides of an edge may be reduced, and thus blur may occur near the edge. We refer the reader to [5, 58] for discussions on the loss of contrast caused by various image processing models using TV regularization.

Partial differential equations (PDEs) and variational approaches have been intensively investigated to enhance the contrast. On the PDE side, some well-known approaches were proposed to tackle the loss of contrast for image enhancement. For example, the shock filter was proposed in [49] to deal with blur-like image degradations, creating strong discontinuities at image edges and flattening the image within homogeneous regions. Afterwards, the shock filter has been generalized in many ways; see, e.g. [3, 65]. Another important example is the forward-and-backward (FAB) diffusion scheme proposed in [30] to simultaneously remove the noise and enhance the contrast. Since then, a number of influential works regarding the FAB diffusion have been conducted; see, e.g. [62, 64, 66]. Despite that different PDE schemes were designed, a common feature of these works is that the *backward diffusion process* is adopted to enhance the contrast of the edges in a concerning image. Since backward diffusion is a classic example of an ill-posed problem [61], most of these PDE schemes sound numerically challenging; we refer the reader to [18, 19, 63] on discretizing and solving these PDEs efficiently. On the variational side, there are attempts to add negative terms into the variational model to maximize the contrast, see, e.g. [28, 50], though their connections with the TV regularization are not considered.

We remark that the enhanced TV model (1.7) has a connection to the backward diffusion approach from the PDE perspective. A detailed explanation in the context of the Euler–Lagrange (E–L) equation in a continuum setting is included in appendix A. Briefly speaking, the term $-\frac{\alpha}{2}\|\nabla X\|_2^2$ generates an additional backward diffusion term $-\alpha\Delta X$ into the E–L equation corresponding to the classic TV regularization. In figure 1, we empirically illustrate that the enhanced TV regularization (1.6) is very effective for some fundamental denoising and deblurring problems. Figure 1 clearly shows that the enhanced TV regularization (1.6) outperforms the original TV regularization in removing noise, reducing loss of contrast, and maintaining smoothness inside homogeneous regions. These compelling performances clearly motivate us to consider theoretical reconstruction guarantees for the enhanced TV model (1.7). Implementation details for reproducing figure 1 are enclosed in appendix B.

In figure 1, we also note that the enhanced TV regularization (1.6) may not ideally overcome another drawback of TV: the *staircase effect*. That is, solutions to TV-based models may have stair-like edges. Many efforts are trying to avoid this effect, including the replacement of the TV regularization with an exponentiation term of it [7], the usage of the infimal convolution of functionals with first- and second-order derivatives as regularizer [16], the addition of some higher-order terms into the E–L equation corresponding to the variational TV model [20], the total generalized variation [8], the usage of some modified infimal convolutions [56, 57] regarding [16], and many others.
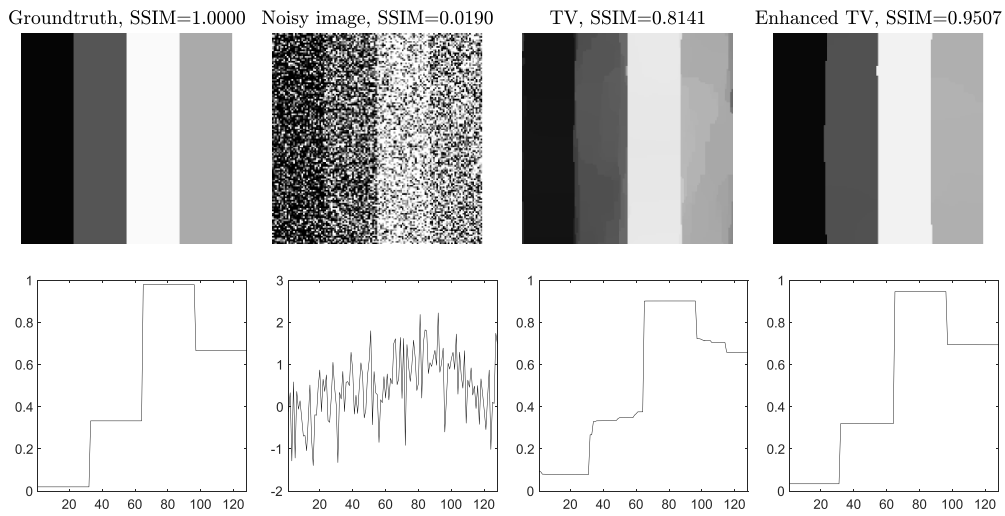
Figure 1. Illustration of the TV and enhanced TV regularization for image denoising. Top row: SSIM values of each image; Bottom row: intensity profiles of each image along the horizontal straight line splitting the image equally.

1.2. A CS view of the enhanced TV regularization

In addition to the PDE and variational perspectives, another interpretation of the enhanced TV regularization (1.6) can be given from the perspective of CS. As previously discussed, an image X is mostly sparse after the gradient transform $\nabla : X \to \nabla X$. Mathematically, CS amounts to minimizing the ℓ_0 norm of the image gradient, i.e. $\|\nabla X\|_0$, which counts the number of non-zero entries of ∇X. To bypass the NP-hard nature of the ℓ_0 norm, we typically seek its alternatives which lead to more tractable models. In the context of image reconstruction, we have the TV regularization [14, 24, 55]

$$\|X\|_{\mathrm{TV}} = \sum_{j,k} |[\nabla X]_{j,k}|,$$

which corresponds to the ℓ_1 penalty in CS. We also have the transformed TV regularization [33]

$$\|X\|_{\mathrm{TTV}} = \sum_{j,k} \frac{(\beta+1)\,|[\nabla X]_{j,k}|}{\beta + |[\nabla X]_{j,k}|}$$

with $\beta > 0$, which corresponds to the transformed ℓ_1 regularization [73] in CS. Moreover, we have the weighted difference of anisotropic and isotropic TV regularization [39]

$$\|X\|_{\mathrm{TV}_a} - \alpha\|X\|_{\mathrm{TV}_i} = \sum_{j,k} \left(|(X_x)_{j,k}| + |(X_y)_{j,k}| - \alpha\sqrt{(X_x)_{j,k}^2 + (X_y)_{j,k}^2} \right)$$

and the minimax concave penalty (MCP) [70, 71]

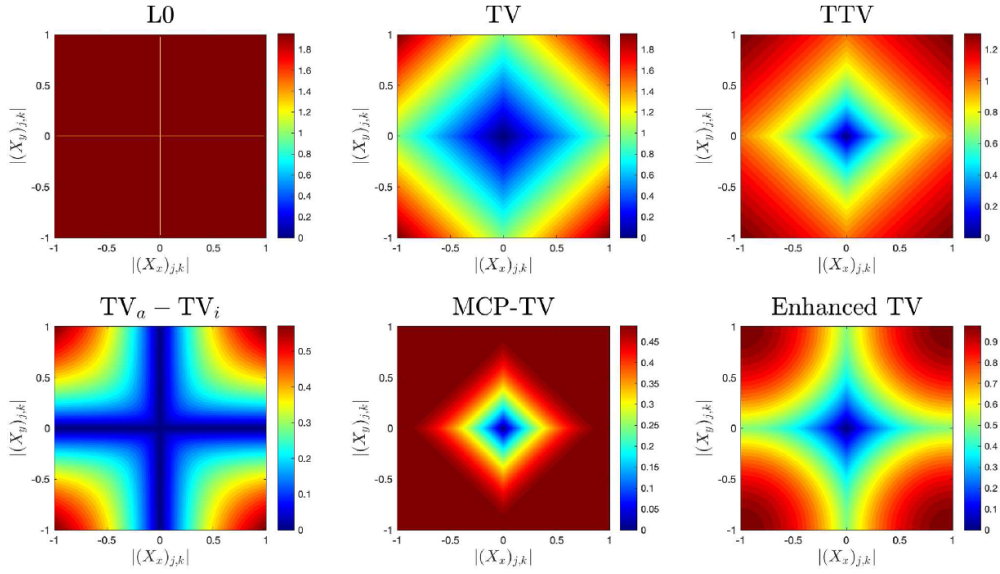$$\|X\|_{\mathrm{MCP-TV}} = \sum_{j,k} \phi_\mu(|[\nabla X]_{j,k}|),$$

Figure 2. Level curves of different regularization terms with anisotropic definitions: $|[\nabla X]_{j,k}| = |(X_x)_{j,k}| + |(X_y)_{j,k}|$.

where $\mu > 0$ and

$$\phi_\mu(x) = \begin{cases} |x| - x^2/(2\mu), & |x| \leqslant \mu, \\ \mu/2, & |x| \geqslant \mu. \end{cases}$$

Our enhanced TV regularization (1.6) can also be written as

$$\mathcal{R}_\alpha(X) = \sum_{j,k} \left[|[\nabla X]_{j,k}| - \frac{\alpha}{2} \left((X_x)_{j,k}^2 + (X_y)_{j,k}^2 \right) \right].$$

In image reconstruction, it is desirable for regularization terms to generate reasonably close approximations of $\|\nabla X\|_0$. Since all the regularization terms mentioned above are separable, we can compare their behavior in terms of each component. We adopt the anisotropic definition $|[\nabla X]_{j,k}| = |(X_x)_{j,k}| + |(X_y)_{j,k}|$, except for the $\text{TV}_a - \alpha \text{TV}_i$ regularization. We set β, μ, and α to 1 for all regularization terms. We plot the level curves of each component with respect to $|(X_x)_{j,k}|$ and $|(X_y)_{j,k}|$ in figure 2. Note that the axes of color bars are intended not to be unified for better visualization. The level lines of the ℓ_0 norm are 0 at the origin, 1 at the axes, and 2 elsewhere. Apart from the convex anisotropic TV regularization, all other regularization terms are non-convex and promote the approximation behavior to the ℓ_0 norm. We observe from figure 2 that all regularization terms preserve 0 at the origin, indicating that they behave similarly within homogeneous regions of images. Additionally, our enhanced TV regularization is closer to the ℓ_0 norm than the other terms at both axes. This suggests that the enhanced TV regularization performs analogously to the ℓ_0 norm around horizontal and vertical edges. In comparison, the $\text{TV}_a - \text{TV}_i$ regularization yields 0 at both axes. Moreover, we note that the transformed TV regularization behaves like plain shrinkage from the anisotropic TV. Furthermore, the truncated definition of the MCP-TV regularization provides it with a closer approximation to the ℓ_0 norm within the non-axis area than other regularization terms, suggesting that this regularization may preserve the behavior of the ℓ_0 norm along oblique edges. However,
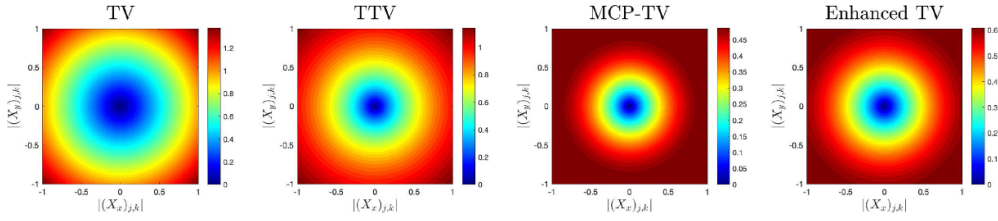
Figure 3. Level curves of different regularization terms with isotropic definitions: $|[\nabla X]_{j,k}| = \sqrt{(X_x)_{j,k}^2 + (X_y)_{j,k}^2}$.

the truncated definition of the MCP-TV may confound oblique edges with horizontal/vertical edges because it has the same values from the end of both axes and non-axis areas. Meanwhile, the enhanced TV regularization performs better than the MCP-TV along the horizontal or vertical edge because the enhanced TV regularization preserves the behavior of the ℓ_0 norm at the end of box axes better than the MCP-TV. These observations suggest that the enhanced TV regularization may be a good proxy of the ℓ_0 norm in the context of image reconstruction. To compare scalar regularization terms and shrinkage operators for corresponding proximal mappings, we refer the reader to our previous work [4].

Since the anisotropic version of the TV regularization is the ℓ_1 norm of the image gradient ∇X when it is viewed as a vector, it may be more suitable for image reconstruction than the isotropic version of the TV regularization. In figure 3, the level curves show that the isotropic TV regularization may be less capable for approximating the ℓ_0 norm than the anisotropic one. Similar results will also be presented in section 5. Hence, we focus on the anisotropic version of the TV regularization in the paper.

1.3. Contributions

In the CS context, it is possible to *exactly* recover a signal if the signal is sparse and its measurements are noise-free; otherwise, we can only establish *stable* recovery guarantees. The term *stable* in this paper is mainly concerned with both inexact sparsity and measurement noise. Our analysis is conducted under the *restricted isometry property* (RIP) framework studied in [11]. We say that a linear operator $\mathcal{A} : \mathbb{C}^{n_1 \times n_2} \to \mathbb{C}^m$ has the RIP of order s and level $\delta \in (0, 1)$ if

$$(1 - \delta)\|X\|_2^2 \leqslant \|\mathcal{A}X\|_2^2 \leqslant (1 + \delta)\|X\|_2^2 \quad \forall s-\text{sparse } X \in \mathbb{C}^{n_1 \times n_2}, \tag{1.8}$$

and the smallest δ for (1.8) is said to be the *restricted isometry constant* (RIC) associated with $\mathcal{A}$.

We first investigate *non-adaptive* subsampled linear RIP measurements of an image $\bar{X} \in \mathbb{C}^{N \times N}$ with noise level $\tau > 0$. By 'non-adaptive,' we mean that the sampling strategy is not designed with specific structures or under certain distributions. In theorem 3.1, we show that the enhanced TV model (1.7) can stably reconstruct an image $\bar{X} \in \mathbb{C}^{N \times N}$ from some non-adaptive subsampled linear RIP measurements which are contaminated by noise, with the RIP order $\mathcal{O}(s)$, the RIP level $\delta < 0.6$, and the noise level $\tau > 0$. Moreover, the required RIP level $\delta < 1/3$ derived in [47] for the TV model (1.2) is weakened to $\delta < 0.6$ for the enhanced TV model (1.7) under the additional condition (3.8) for the parameter α. We also show in theorem 3.2 that the reconstruction error bound in theorem 3.1 can be further improved if more measurements are allowed.

The above reconstruction guarantees for non-adaptive measurements require the sub-sampled measurements and the Haar wavelet basis to be sufficiently incoherent. This requirement is satisfied by many kinds of measurements except for the Fourier frequency measurements, because low-order wavelets and Fourier measurements are highly correlated, as analyzed in [36]. Fourier measurements play essential roles in many imaging tasks. For example, as discussed in [26, 36], the measurement process of various image processing procedures such as radar, sonar, and computer tomography can be modeled (with appropriate approximation and discretization) by taking samples from weighted discrete Fourier transforms. It is also known (see, e.g. [41]) that measurements taken for magnetic resonance imaging (MRI) can be well modeled as Fourier coefficients of the desired image.

On the other hand, many empirical pieces of evidence, including the first works [40, 41] for CS MRI, have shown that better reconstruction quality is possible by subsampling Fourier frequency measurements with a preference for low frequencies over high frequencies. Thus, we follow the *density-variable* sampling strategy proposed in [36] and choose Fourier measurements randomly according to an *inverse square law density*. We show that from at least $m \gtrsim s \log^3(s) \log^5(N)$ such subsampled Fourier measurements with $s \gtrsim \log(N)$, the enhanced TV model (1.7) reconstructs an unknown image $\bar{X}$ stably with high probabilities. We also show that the least amount of Fourier measurements required by the enhanced TV model (1.7) is only $(0.6/(1/3))^{-2} \approx 30.86\%$ of that by the TV model (1.2) as established in [36].

1.4. Related works

We briefly review some TV-related works on image reconstruction. The reconstruction of a one-dimensional image in $\mathbb{C}^N$ with an exactly s-sparse gradient from noise-free, uniformly sub-sampled Fourier measurements was considered in [10], without stability analysis concerning the inexact sparsity or noise. It was shown that this one-dimensional image could be recovered exactly by solving the corresponding TV model with high probabilities, provided that the number of measurements m satisfies $m \gtrsim s \log(N)$. The reconstruction of a one-dimensional image using noisy measurements was then considered in [9]. The stability of the reconstruction of approximately sparse images from noisy measurements was first shown in [47] for two-dimensional images and soon extended to higher-dimensional cases in [46]. More specifically, it was asserted in [47] that, from some non-adaptive subsampled linear RIP measurements of an image $\bar{X} \in \mathbb{C}^{N \times N}$ with the RIP order $\mathcal{O}(s)$, the RIP level $\delta < 1/3$, and the noise level $\tau > 0$, the solution X^{opt} to the TV model (1.2) satisfies

$$\|\bar{X} - X^{\mathrm{opt}}\|_2 \lesssim \log\left(\frac{N^2}{s}\right)\left(\frac{\|\nabla\bar{X} - (\nabla\bar{X})_s\|_1}{\sqrt{s}} + \tau\right), \tag{1.9}$$

where $(\nabla\bar{X})_s$ is the best s-sparse approximation to the discrete gradient ∇X. Moreover, with more measurements, it was shown in [47] that the log factor in the bound (1.9) could be removed, and thus the bound (1.9) can be improved as

$$\|\bar{X} - X^{\mathrm{opt}}\|_2 \lesssim \frac{\|\nabla\bar{X} - (\nabla\bar{X})_s\|_1}{\sqrt{s}} + \tau. \tag{1.10}$$

In comparison with the bound (1.10), the reconstruction error bound for the enhanced TV model (1.7) in theorem 3.2 is tighter if the level of noise τ is relatively large and the number of measurements m is limited. More discussions can be found in section 3.3. Besides, the RIP level is assumed to satisfy $\delta < 1/3$ in [47] for the TV model (1.2), while we weaken it to $\delta < 0.6$ for the enhanced TV model (1.7). Though $\delta < 1/3$ can be improved, as remarked in [47], the reconstruction error bounds (1.9) and (1.10) for the TV model (1.2) tend to be

infinity if $\delta \to 0.6$ (cf the proof of proposition 3 in [47]). On the other hand, the bounds in theorems 3.1 and 3.2 for the enhanced TV model (1.7) are still reasonably valid when $\delta \to 0.6$; meanwhile, the upper bound required for α tends to be 0 correspondingly. Thus, as $\delta \to 0.6$, the bounds (3.11) and (3.13) in theorems 3.1 and 3.2 for the enhanced TV model (1.7) assert the stability of the TV model (1.2) in image reconstruction from a few linear RIP measurements.

As mentioned, guarantees for non-adaptive measurements require the subsampled measurements and the Haar wavelet basis to be sufficiently incoherent. Thus, the mentioned guarantees in [46, 47] cannot be directly applied to the situation of Fourier measurements. The first results on image reconstruction from Fourier measurements were derived in [36, 51], in which *uniform* and *non-uniform*[3] reconstruction guarantees are considered, respectively. More specifically, the approach in [36] requires a larger number of measurements than [51], while its reconstruction error bound is sharper than that in [51]. In [36], uniform reconstruction guarantees were derived for two-dimensional images from noisy Fourier measurements, chosen randomly according to an inverse square law density. Specifically, from at least $m \gtrsim s \log^3(s) \log^5(N)$ such subsampled Fourier measurements with $s \gtrsim \log(N)$, the reconstruction error bound for the TV model (1.2) was derived in the same form of (1.10). We refer to, e.g. [1, 2, 34], for more discussions. As we focus on the uniform reconstruction from non-adaptive measurements, we follow the approach in [36] to consider Fourier measurements.

1.5. Outline

The rest of this paper is organized as follows. In the next section, we summarize some notation and technical backgrounds. In section 3, we establish stable image reconstruction guarantees for the enhanced TV model (1.7) from non-adaptive subsampled linear RIP measurements and variable-density subsampled Fourier measurements, respectively. Proofs of the results in section 3 are presented in section 4. In section 5, we report some numerical results when the enhanced TV model (1.7) is applied to some image reconstruction problems. Different kinds of images with subsampled Fourier measurements are tested. Finally, we make some conclusions in section 6.

2. Preliminaries

We first summarize some notation and recall some preliminary technical backgrounds.

2.1. Notation

For any $x, y \in \mathbb{R}^n$, let $\langle x, y \rangle = x^\mathrm{T} y$ be their inner product, and $\|x\|_p$ $(p \geqslant 1)$ be the usual ℓ_p-norm of x. For a matrix $X \in \mathbb{R}^{m \times n}$, let $\mathrm{supp}(X) := \{(j, k) : X_{j,k} \neq 0\}$ be the support of X, and $\|X\|_0$ be the cardinality of $\mathrm{supp}(X)$. X is said to be s-sparse if $\|X\|_0 \leqslant s$. Let

$$\|X\|_{p,q} := \left(\sum_{j=1}^{m} \left(\sum_{k=1}^{n} |X_{j,k}|^p \right)^{q/p} \right)^{1/q}$$

---

[3] In the context of compressed sensing, a *uniform reconstruction guarantee* indicates that a single random draw of a given measurement operator suffices to recover all sparse or approximately sparse vectors. In contrast, a *non-uniform recovery guarantee* states that a single random draw is sufficient for recovery of a fixed vector.

be the entry-wise $\ell_{p,q}$ norm $(p,q \geqslant 1)$ of X. If $p=q$, $\|X\|_{p,p}$ is denoted by $\|X\|_p$ for short. In particular, the $\ell_{2,2}$ norm is also known as the Frobenius norm, which is induced by the inner product $\langle X,Y \rangle := \sum_{j=1}^m \sum_{k=1}^n X_{i,j} Y_{i,j} = \mathrm{tr}(XY^*)$ for any $X,Y \in \mathbb{C}^{m \times n}$, where X^* denotes the adjoint of the matrix X. For an index set $S \subset \{1,2,\ldots,m\} \times \{1,2,\ldots,n\}$, let $X_S \in \mathbb{R}^{m \times n}$ be the matrix with the same entries as X on indices S and zero entries on indices S^c. The only exception is $\mathcal{F}_\Omega$. We denote by $\mathcal{F}_\Omega$ the restriction of the bivariate discrete Fourier transform $\mathcal{F}$ to a subset $\Omega \subset \{-N/2+1,\ldots,N/2\}^2$. Logarithm without indicating base is with respect to base 2. For matrices or vectors x and y of the same dimension, $x \circ y$ denotes the Hadamard (entry-wise) product between x and y. We use the notation $a \lesssim b$ to mean that there exists $C > 0$ such that $a \leqslant Cb$, and likewise for the symbol $\gtrsim$.

2.2. Haar wavelet system

The Haar wavelet system provides a simple yet powerful sparse approximation of digital images. The following descriptions on this system can be found in, e.g. [47]. The *univariate* Haar wavelet system is a complete orthonormal system of square-integrable functions on the unit interval, consisting of the constant function

$$H^0(t) = \begin{cases} 1, & 0 \leqslant t < 1, \\ 0, & \text{otherwise,} \end{cases}$$

the mother wavelet

$$H^1(t) = \begin{cases} 1, & 0 \leqslant t < 1/2, \\ -1, & 1/2 \leqslant t < 1, \end{cases}$$

and the dyadic dilations and translates of the mother wavelet $H_{j,k}(t) = 2^{j/2} H^1(2^j t - k)$, $j \in \mathbb{N}$, $0 \leqslant k < 2^j$. The *bivariate* Haar wavelet system is an orthonormal system for the space $L_2(Q)$ of square-integrable functions on the unit square $Q = [0,1)^2$, and it is derived from the univariate Haar system by tensor product. The bivariate Haar system consists of the constant function and all functions

$$x = (u,v), \quad H_{j,k}^\ell(x) = 2^j H^\ell(2^j x - k),$$

for $j \geqslant 0$, $k \in \mathbb{Z}^2 \cap 2^j Q$, and $\ell \in V := \{\{0,1\},\{1,0\},\{1,1\}\}$, where

$$H^\ell(u,v) = H^{\ell_1}(u) H^{\ell_2}(v)$$

and $\ell = (\ell_1,\ell_2) \in V$. Discrete images are isometric to the space $\Sigma_N \subset L_2(Q)$ of piecewise-constant functions

$$\Sigma_N = \left\{ f \in L_2(Q) : f(u,v) = c_{j,k}, \frac{j-1}{N} \leqslant u < \frac{j}{N}, \frac{k-1}{N} \leqslant v < \frac{k}{N} \right\} \tag{2.1}$$

with $c_{j,k} = N X_{j,k}$. If $N = 2^n$, then the bivariate Haar basis is restricted to the $2^n \times 2^n = N^2$ basis functions $\{H_{j,k}^\ell : j \leqslant n-1\}$ and identified as some discrete images $h_{j,k}^\ell$ via (2.1) forms an orthonormal basis for $\mathbb{C}^{N \times N}$. For any given $\ell = (\ell_1,\ell_2) \in V$, we denote by $\mathcal{H}$ the bivariate Haar transform $X \mapsto (\langle X, h_{j,k}^\ell \rangle)_{j,k}$. By a slight abuse of notation, we also denote by $\mathcal{H}$ the unitary matrix representing this bivariate Haar transform. That is, we denote by $\mathcal{H}X$ the matrix product that generates $(\langle X, h_{j,k}^\ell \rangle)_{j,k}$.

Some properties of the bivariate Haar wavelet system are summarized below, and the proofs can be found in [47].

Lemma 2.1. *Suppose $X \in \mathbb{C}^{N \times N}$ is mean-zero, and let $c_{(k)}(X)$ be the bivariate Haar coefficient of X having the kth largest magnitude, or the entry of the bivariate Haar transform $\mathcal{H}X$ having the kth largest magnitude. Then, for all $k \geqslant 1$, $|c_{(k)}(X)| \leqslant \tilde{C} \|\nabla X\|_1 / k$, where $\tilde{C} > 0$ is some constant.*

Lemma 2.2. *Let $N = 2^n$. For any indices (j, k) and $(j, k + 1)$, there are at most $6n$ bivariate Haar wavelets which are not constant on these indices, i.e. $|h_{j,k}^{\ell}(j, k+1) - h_{j,k}^{\ell}(j, k)| > 0$.*

Lemma 2.3. *The bivariate Haar wavelets satisfy $\|\nabla h_{j,k}^{\ell}\|_1 \leqslant 8$ for all j, k, ℓ.*

2.3. Discrete Fourier system

In addition to general RIP measurements, we particularly investigate Fourier measurements. Let $N = 2^n$ be a power of 2, where $n \in \mathbb{N}^+$. The following facts of Fourier basis and transform in the context of imaging can be found in, e.g. [36]. The *univariate* discrete Fourier basis of $\mathbb{C}^N$ consists of vectors

$$\varphi_k(t) = \frac{1}{\sqrt{N}} e^{i2\pi tk/N}, \quad -N/2 + 1 \leqslant t \leqslant N/2,$$

indexed by the discrete frequencies in the range of $-N/2 + 1 \leqslant k \leqslant N/2$. The *bivariate* discrete Fourier basis of $\mathbb{C}^{N \times N}$ is a tensor product of univariate bases, i.e.

$$\varphi_{j,k}(u, v) = \frac{1}{N} e^{i2\pi (ju+kv)/N}, \quad -N/2 + 1 \leqslant u, v \leqslant N/2,$$

indexed by the discrete frequencies in the range of $-N/2 + 1 \leqslant j, k \leqslant N/2$.

We denote by $\mathcal{F}$ the bivariate discrete Fourier transform $X \mapsto (\langle X, \varphi_{k_1,k_2} \rangle)_{k_1,k_2}$. Again, by a slight abuse of notation, we denote by $\mathcal{F}$ the unitary matrix representing this linear map. That is, we denote by $\mathcal{F}X$ the matrix product that generates $(\langle X, \varphi_{k_1,k_2} \rangle)_{k_1,k_2}$. Moreover, since limited measurements are considered, we denote by $\mathcal{F}_\Omega$ the restriction of $\mathcal{F}$ to a subset of frequencies $\Omega \subset \{-N/2 + 1, \ldots, N/2\}^2$.

3. Main results

We now establish reconstruction guarantees for the enhanced TV model (1.7) from non-adaptive linear RIP measurements and variable-density Fourier measurements, respectively. The following proposition generalizes theorem 4.1 in [4] for signal recovery, and it allows us to bound the norm of an image D when it is close to the null space of an RIP operator.

Proposition 3.1. *Let $\gamma \geqslant 1$, $k > 0$, $\delta < 0.6$, $\beta_1 > 0$, $\beta_2 > 0$, and $\varepsilon \geqslant 0$, and let $\mathcal{A}$ be some linear operator $\mathcal{A} : \mathbb{C}^{n_1 \times n_2} \to \mathbb{C}^{\tilde{m}}$, where $n_1, n_2, \tilde{m} \in \mathbb{N}^+$. Suppose that $\mathcal{A}$ has the RIP of order $k + 4k\gamma^2$ and level δ, and that the image $D \in \mathbb{C}^{N \times N}$ satisfies the tube constraint*

$$\|\mathcal{A}D\|_2 \leqslant \varepsilon. \tag{3.1}$$

Suppose further that for a subset S of cardinality $|S| \leqslant k$, D satisfies the cone constraint

$$\|D_{S^c}\|_1 \leqslant \gamma \|D_S\|_1 - \frac{\beta_1}{2} \|D\|_2^2 + \sigma + \beta_2 \langle E_1, E_2 \rangle, \tag{3.2}$$

where E_1, E_2 could be scalars, vectors, or matrices, and E_2 is assumed to satisfy $\|E_2\|_2 = \|D\|_2$. Here $\|\cdot\|_2$ denotes the absolute value for scalars, the usual ℓ_2 vector norm for vectors, and

the $\ell_{2,2}$ norm (Frobenius norm) for matrices. If β_2 satisfies the posterior verification

$$\beta_2 \leqslant \frac{\gamma\sqrt{k}}{2K_2\|E_1\|_2}, \tag{3.3}$$

then it holds that

$$\|D\|_2 \leqslant \sqrt{\frac{\gamma\sqrt{k}K_1}{\beta_1 K_2}\varepsilon + \frac{2}{\beta_1}\sigma} \lesssim \sqrt{\frac{\gamma\sqrt{k}}{\beta_1}\varepsilon + \frac{1}{\beta_1}\sigma}, \tag{3.4}$$

where

$$K_1 := \frac{3}{2\sqrt{1-\delta} - \sqrt{1+\delta}} \quad \text{and} \quad K_2 := \frac{\sqrt{1+\delta}}{4}\left(K_1 + \frac{1}{\sqrt{1+\delta}}\right).$$

Furthermore, we have

$$\|D\|_1 \leqslant \frac{(2K_2+1)\gamma\sqrt{k} + 2K_2\sqrt{k}}{2K_2}\sqrt{\frac{\gamma\sqrt{k}K_1}{\beta_1 K_2}\varepsilon + \frac{2}{\beta_1}\sigma} + \sigma$$

$$\lesssim \gamma\sqrt{k}\sqrt{\frac{\gamma\sqrt{k}}{\beta_1}\varepsilon + \frac{1}{\beta_1}\sigma} + \sigma. \tag{3.5}$$

Corollary 3.1. *There is a linear term of σ in (3.5). If $\|D\|_2 \geqslant \sqrt{2\sigma/\beta_1}$, which is compatible with (3.4), then this linear term can be removed. This corollary will be proved after proposition 3.1.*

Remark 3.1. In the proof of proposition 3.1, we need to ensure $\sqrt{1-\delta} - \sqrt{1+\delta}/2 > 0$, and this is where the requirement $\delta < 0.6$ for the RIP level stems from. Since

$$\lim_{\delta \to 0.6} \frac{K_1}{K_2} = \lim_{\delta \to 0.6} \frac{4}{\sqrt{1+\delta} + 1/K_1} = 10, \tag{3.6}$$

the bounds on $\|D\|_2$ and $\|D\|_1$ are still reasonable as $\delta \to 0.6$. As the whole analysis below rests upon proposition 3.1, this fact (3.6) suggests that the following reconstruction error bounds (3.11), (3.13) and (3.18) are all reasonable as $\delta \to 0.6$.

Remark 3.2. If $\mathcal{A}$ is assumed to have the RIP of order $5k\gamma^2 \geqslant k + 4k\gamma^2$, then proposition 3.1 still holds. Thus, we assume the order $5k\gamma^2$ for simplicity in the following theorems.

For any image $X \in \mathbb{C}^{N\times N}$, its derivatives X_x and X_y belong to $\mathbb{C}^{(N-1)\times N}$ and $\mathbb{C}^{N\times(N-1)}$, respectively. Thus, it is convenient to consider the matrices Π_0 and Π^0 obtained from a matrix Π by concatenating a row of zeros to the bottom and top of Π, respectively. More concretely, for a matrix $\Pi \in \mathbb{C}^{(N-1)\times N}$, we denote by $\Pi^0 \in \mathbb{C}^{N\times N}$ the augmented matrix with entries

$$(\Pi^0)_{j,k} = \begin{cases} 0, & j = 1, \\ \Pi_{j-1,k}, & 2 \leqslant j \leqslant N. \end{cases}$$

Similarly, we denote by $\Pi_0 \in \mathbb{C}^{N\times N}$ the matrix constructed from adding a row of zeros to the bottom of Π. For a linear operator $\mathcal{A}: \mathbb{C}^{(N-1)\times N} \to \mathbb{C}^m$ with $[\mathcal{A}(X)]_j = \langle A_j, X\rangle$, we denote by $\mathcal{A}^0: \mathbb{C}^{N\times N} \to \mathbb{C}^m$ the linear operator with $[\mathcal{A}^0(X)]_j = \langle A_j^0, X\rangle$. We denote by $\mathcal{A}_0: \mathbb{C}^{N\times N} \to \mathbb{C}^m$ similarly. It was shown in [47] that the entire image and its gradients could be related as follows.

Lemma 3.1 ([47]). *Given $X \in \mathbb{C}^{N\times N}$ and $\Pi \in \mathbb{C}^{(N-1)\times N}$,*

$$\langle \Pi, X_x\rangle = \langle \Pi^0, X\rangle - \langle \Pi_0, X\rangle \quad \text{and} \quad \langle \Pi, X_y^T\rangle = \langle \Pi^0, X^T\rangle - \langle \Pi_0, X^T\rangle,$$

where X^T denotes the (non-conjugate) transpose of the matrix X.

3.1. Reconstruction from non-adaptive linear RIP measurements

We are prepared to state our first result on stable image reconstruction from non-adaptive linear RIP measurements.

Theorem 3.1. *Let $N = 2^n$ be a power of two, where $n \in \mathbb{N}^+$. Let $\mathcal{A} : \mathbb{C}^{(N-1) \times N} \to \mathbb{C}^{m_1}$ and $\mathcal{A}' : \mathbb{C}^{(N-1) \times N} \to \mathbb{C}^{m_1}$ be such that the concatenated operator $[\mathcal{A}, \mathcal{A}']$ has the RIP of order $5s$ and level $\delta < 0.6$. Let $\mathcal{H} : \mathbb{C}^{N \times N} \to \mathbb{C}^{N \times N}$ be the orthonormal bivariate Haar wavelet transform, and $\mathcal{B} : \mathbb{C}^{N \times N} \to \mathbb{C}^{m_2}$ be such that the composite operator $\mathcal{B}\mathcal{H}^* : \mathbb{C}^{N \times N} \to \mathbb{C}^{m_2}$ has the RIP of order $2s + 1$ and level $\delta < 1$. Let $m = 4m_1 + m_2$, and consider the linear operator $\mathcal{M} : \mathbb{C}^{N \times N} \to \mathbb{C}^m$ with components*

$$\mathcal{M}(X) = \left(\mathcal{A}^0(X), \mathcal{A}_0(X), \mathcal{A}'^0(X^T), \mathcal{A}'_0(X^T), \mathcal{B}(X) \right). \tag{3.7}$$

Let $\bar{X} \in \mathbb{C}^{N \times N}$ be an image and X^{opt} the solution to the enhanced TV model (1.7) with $\mathcal{M}$ defined as (3.7). If α satisfies

$$\alpha \leqslant \frac{\sqrt{s}}{2K_2 \|\nabla X^{\text{opt}}\|_2}, \tag{3.8}$$

then we have the stable gradient reconstruction results

$$\|\nabla \bar{X} - \nabla X^{\text{opt}}\|_2 \lesssim \sqrt{\frac{\sqrt{s}}{\alpha} \tau + \frac{1}{\alpha} \|\nabla \bar{X} - (\nabla \bar{X})_s\|_1} \tag{3.9}$$

and

$$\|\nabla \bar{X} - \nabla X^{\text{opt}}\|_1 \lesssim \sqrt{s} \sqrt{\frac{\sqrt{s}}{\alpha} \tau + \frac{1}{\alpha} \|\nabla \bar{X} - (\nabla \bar{X})_s\|_1} + \|\nabla \bar{X} - (\nabla \bar{X})_s\|_1, \tag{3.10}$$

and the stable image reconstruction result

$$\begin{aligned}
\|\bar{X} - X^{\text{opt}}\|_2 &\lesssim \log\left(\frac{N^2}{s}\right) \sqrt{\frac{\sqrt{s}}{\alpha} \tau + \frac{1}{\alpha} \|\nabla \bar{X} - (\nabla \bar{X})_s\|_1} \\
&\quad + \log\left(\frac{N^2}{s}\right) \frac{\|\nabla \bar{X} - (\nabla \bar{X})_s\|_1}{\sqrt{s}} + \tau.
\end{aligned} \tag{3.11}$$

Corollary 3.2. *Enlightened by corollary 3.1, if*

$$\|\nabla \bar{X} - \nabla X^{\text{opt}}\|_2 \geqslant \sqrt{\frac{2}{\alpha} \|\nabla \bar{X} - (\nabla \bar{X})_s\|_1},$$

which is compatible with (3.9), then the linear term $\|\nabla \bar{X} - (\nabla \bar{X})_s\|_1$ in (3.10) and hence the term $\log\left(\frac{N^2}{s}\right) \frac{\|\nabla \bar{X} - (\nabla \bar{X})_s\|_1}{\sqrt{s}}$ in (3.11) can be removed. This corollary will be proved after theorem 3.1.

Remark 3.3. The proof of theorem 3.1 is inspired by the proof in [47] for the TV model (1.2), in which it was conjectured that the $4m_1$ measurements derived from $\mathcal{A}$ in the construction (3.7) of $\mathcal{M}$ are artifacts of the proof. The components $\mathcal{A}^0(X)$, $\mathcal{A}_0(X)$, $\mathcal{A}'^0(X^{\text{T}})$, and $\mathcal{A}'_0(X^{\text{T}})$ are only used for deriving the stable gradient reconstruction bounds (3.9) and (3.10). On the other hand, component $\mathcal{B}(X)$ only helps us derive the bound (3.11) from (3.9) and (3.10).

If more measurements are allowed, then the bound (3.11) can be further improved, the requirement (3.8) on α can be relaxed, and the artificial components in $\mathcal{M}$ can be removed.

Theorem 3.2. *Let $N = 2^n$ be a power of two, where $n \in \mathbb{N}^+$. Let $\mathcal{H} : \mathbb{C}^{N \times N} \to \mathbb{C}^{N \times N}$ be the orthonormal bivariate Haar wavelet transform, and $\mathcal{M} : \mathbb{C}^{N \times N} \to \mathbb{C}^m$ be such that the composite operator $\mathcal{M}\mathcal{H}^* : \mathbb{C}^{N \times N} \to \mathbb{C}^m$ has the RIP of order $Cs \log^3(N)$ and level $\delta < 0.6$. Let*

$\bar{X} \in \mathbb{C}^{N \times N}$ *be a mean-zero image or an image containing some zero-valued pixels, and* X^{opt} *be the solution to the enhanced TV model (1.7). If* α *satisfies*

$$\alpha \leqslant \frac{\sqrt{48s \log(N)}}{K_2 \|\nabla X^{\text{opt}}\|_2}, \tag{3.12}$$

then we have

$$\|\bar{X} - X^{\text{opt}}\|_2 \lesssim \sqrt{\frac{\sqrt{s}}{\alpha} \tau + \frac{1}{\alpha} \|\nabla \bar{X} - (\nabla \bar{X})_s\|_1}. \tag{3.13}$$

Remark 3.4. The RIP requirements in both theorems above indicate that the linear measurements should be generated from standard RIP matrix ensembles, which are incoherent with the Haar wavelet system. Many classes of random matrices can be used to generate RIP matrix ensembles. For example, a matrix in $\mathbb{R}^{m \times N^2}$ with i.i.d. normalized Gaussian random entries has a small RIP constant $\delta_s < c$ with high probabilities if $m \gtrsim c^{-2} s \log(N^2/s)$, as shown in [11]. Similar results were extended to sub-Gaussian matrices in [43]. If $m \gtrsim s \log^4(N)$, then it was proved in [12, 54] that the RIP holds with overwhelming probabilities for a partial Fourier matrix $\mathcal{F}_\Omega \in \mathbb{R}^{m \times N^2}$. The RIP also holds for randomly generated circulant matrices (see [52]) and randomly subsampled bounded orthonormal systems (see [53]). Most of these mentioned measurements are incoherent with the Haar wavelet system, but the partial Fourier matrix with uniformly subsampled rows is an exception. Thus, some specific sampling strategies for Fourier measurements should be considered. For example, it was asserted in [35] that $\mathcal{F}_\Omega \in \mathbb{R}^{m \times N^2}$ with $m \gtrsim s \log^4(N)$ and *randomized column signs* has the RIP; it was also shown in [36] that $\mathcal{F}_\Omega$ with rows subsampled according to some power-law densities is incoherent with the Haar wavelet system after preconditioning.

3.2. Reconstruction from variable-density Fourier measurements

As shown in [36], if the measurements are sampled according to appropriate power-law densities, then they are incoherent with the Haar wavelet system. We consider a particular variable-density sampling strategy proposed in [36] and derive a partial stable image reconstruction theorem tailored for Fourier measurements. Following the idea of [36], our guarantees are based on a *weighted ℓ_2-norm* in measuring noise such that high-frequency measurements have a higher sensitivity to noise; that is, the ℓ_2-norm in the constraint $\|\mathcal{M}X - y\|_2 \leqslant \tau$ of the enhanced TV model (1.7) is replaced by a weighted ℓ_2-norm model. For the particular scenario with Fourier measurements, the general linear operator $\mathcal{M}$ is specified as $\mathcal{F}_\Omega$, which is the restriction of the Fourier transform matrix to a set Ω of frequencies as defined in section 2.3.

Theorem 3.3. *Let $N = 2^n$ be a power of 2, where $n \in \mathbb{N}^+$. Let m and s satisfy $s \gtrsim \log(N)$ and*

$$m \gtrsim s \log^3(s) \log^5(N). \tag{3.14}$$

Select m frequencies $\{(\omega_1^j, \omega_2^j)\}_{j=1}^m \subset \{-N/1 + 2, \ldots, N/2\}^2$ i.i.d. according to

$$\mathbb{P}[(\omega_1^j, \omega_2^j) = (k_1, k_2)] = C_N \min\left(C, \frac{1}{k_1^2 + k_2^2}\right) =: \eta(k_1, k_2) \tag{3.15}$$

for $-N/2 + 1 \leqslant k_1, k_2 \leqslant N/2$, where C is an absolute constant and C_N is chosen such that η is a probability distribution. Consider the weight vector $\rho = (\rho_j)_{j=1}^m$ with $\rho_j = [1/\eta(\omega_1^j, \omega_2^j)]^{1/2}$. Then we have the following assertion for all mean-zero or zero-valued pixel-containing images

$\bar{X} \in \mathbb{C}^{N \times N}$ *with probability exceeding* $1 - N^{-C\log^3(s)}$: *given noisy partial Fourier measurements* $b = \mathcal{F}_\Omega \bar{X} + e$, *if*

$$\alpha \leqslant \frac{\sqrt{48s\log(N)}}{K_2\|\nabla X^{\mathrm{opt}}\|_2}, \tag{3.16}$$

then the solution X^{opt} *to the model*

$$\min_{X \in \mathbb{C}^{N \times N}} \|\nabla X\|_1 - \frac{\alpha}{2}\|\nabla X\|_2^2 \quad s.t. \quad \|\rho \circ (\mathcal{F}_\Omega X - b)\|_2 \leqslant \tau\sqrt{m} \tag{3.17}$$

satisfies

$$\|\bar{X} - X^{\mathrm{opt}}\|_2 \lesssim \sqrt{\frac{\sqrt{s}}{\alpha}\tau + \frac{1}{\alpha}\|\nabla\bar{X} - (\nabla\bar{X})_s\|_1}. \tag{3.18}$$

3.3. Further discussion

We supplement more details about the theoretical results presented in sections 3.1 and 3.2.

The *a posterior* verification on α. Three conditions (3.8), (3.12) and (3.16) on α are required in theorems 3.1, 3.2 and 3.3, respectively. Determining the value of α is possible only if we have *a priori* estimation on $\|X^{\mathrm{opt}}\|_2$. Thus, these conditions can be interpreted as *a posterior* verification because they can be verified once X^{opt} is obtained by solving the model (1.7). In practice, we solve the model (1.7) numerically and thus obtain an approximate solution, denoted by X^*, subject to a preset accuracy $\epsilon > 0$. That is, $\|X^{\mathrm{opt}} - X^*\|_2 \leqslant \epsilon$. Then, if

$$\alpha \leqslant \frac{\sqrt{s}}{2K_2(\|\nabla X^*\|_2 + \epsilon)},$$

then (3.8) is guaranteed; if

$$\alpha \leqslant \frac{\sqrt{48s\log(N)}}{K_2(\|\nabla X^*\|_2 + \epsilon)},$$

then (3.12) and (3.16) are satisfied.

The RIP level $\delta < 0.6$ in theorems 3.1 and 3.2. The bound 0.6 is sharp, as we need to ensure $\sqrt{1-\delta} - \sqrt{1+\delta}/2 > 0$ (cf proof in section 4.1). For the reconstruction guarantees derived in [47] for the TV model (1.2), the level is assumed to satisfy $\delta < 1/3$, and it is not sharp as remarked in [47]. Though $\delta < 1/3$ can be improved, the reconstruction error bound in [47] for the TV model (1.2) tends to be infinity if $\delta \to 0.6$. In light of remark 3.1, the bounds (3.11) and (3.13) are still valid in this case, and the upper bound required for α tends to 0 correspondingly with consideration of the behavior of K_2. That is, theorems 3.1 and 3.2 can guarantee the stability of the TV model (1.2) when $\delta \to 0.6$, resulting in reconstruction error bounds in forms of (3.11) and (3.13).

The required amount *m* of Fourier measurements in theorem 3.3. The RIP level δ does not appear explicitly in theorem 3.3, while we shall assume $m \gtrsim s\delta^{-2}\log^3(s)\log^5(N)$ and the constant δ is eliminated in such an inequality with $\gtrsim$; see our proof in section 4.4. The least required amount *m* for the TV model (1.2) shall also satisfy this relation with s, N, and δ, as proved in [36]. Since the upper bound on the RIP level δ is enlarged from 1/3 for the TV model (1.2) (see [36]) to 0.6 for the enhanced TV model (1.7), the least amount of Fourier measurements required for the enhanced TV model (1.7) should be $(0.6/(1/3))^{-2} \approx 30.86\%$ of the least amount of Fourier measurements required in [36] for the TV model (1.2).

Inconsistency when $\alpha \to 0$. The enhanced TV regularization (1.6) tends to be the anisotropic TV term as $\alpha \to 0$. At the same time, the reconstruction error bounds (3.11), (3.13),

and (3.18) do not reduce to the corresponding bounds (1.9) and (1.10) for the TV model (1.2). Note that the bounds (3.13) and (3.18) are of the same form. To explain this inconsistency, note that proposition 3.1 is a pillar of the proofs of theorems 3.1, 3.2, and 3.3. In contrast, the proof for the TV model (1.2) in [47] relies on the following fact: if D satisfies the tube constraint (3.1) and the cone constraint $\|D_{S^c}\|_1 \leqslant \gamma\|D_S\|_1 + \sigma$, then it was shown in [47] that

$$\|D\|_2 \lesssim \frac{\sigma}{\gamma\sqrt{k}} + \varepsilon \quad \text{and} \quad \|D\|_1 \lesssim \sigma + \gamma\sqrt{k}\varepsilon. \tag{3.19}$$

Indeed, the left-hand side of the estimation (4.2) in the proof of proposition 3.1 contains a quadratic term $\|D\|_2^2$ and a linear term $\|D\|_2$, and only the linear term remains if $\beta_1, \beta_2 \to 0$, which then leads to the same result as (3.19). However, in the proof of proposition 3.1, we remove this linear term and keep the quadratic term, and hence the obtained result cannot be reduced to the result (3.19) as $\beta_1, \beta_2 \to 0$. Such an inconsistent situation is also encountered by the springback model in [4].

Comparison between (1.10) and (3.13). We are interested in whether or not the bound (3.13) (as well as the bound (3.18), which shares the same form as (3.13)) can be tighter than (1.10) in the sense of

$$\sqrt{\frac{\sqrt{s}}{\alpha}\tau + \frac{1}{\alpha}\|\nabla\bar{X} - (\nabla\bar{X})_s\|_1} \lesssim \frac{\|\nabla\bar{X} - (\nabla\bar{X})_s\|_1}{\sqrt{s}} + \tau, \tag{3.20}$$

with a given $\alpha > 0$. If the image $\bar{X}$ is known to have an s-sparse gradient, then the comparison (3.20) is reduced to $\sqrt{s} \lesssim \alpha\tau$. As s is fixed in this scenario, we can claim that the estimation (3.13) is tighter than the estimation (1.10) in the sense of (3.20) if $\tau \gtrsim \sqrt{s}/\alpha$, i.e. the level of noise τ is *relatively large*. If the sparsity of $\nabla\bar{X}$ is not assumed, but the linear measurements are noise-free, i.e. $\tau = 0$, then the comparison (3.20) is reduced to

$$s/\|\nabla\bar{X} - (\nabla\bar{X})_s\|_1 \lesssim \alpha, \tag{3.21}$$

in which the left-hand side of (3.21) is an increasing function of s. In order to discern the scenario where (3.21) holds, a key fact from remark 3.4 should be noticed: for RIP measurements mentioned there, a small number m of measurements admits an RIP with a small s. The bound $\mathcal{O}(s\log(N^2/s))$ for Gaussian measurements appears not to be monotonic with respect to s. On the other hand, with the implicit constant factors derived in [54], this bound is indeed monotonically increasing with respect to s. Thus, if *the number of measurements m is limited*, which only renders an RIP with a small s, then (3.21) holds. This situation coincides with the intuition that, as the term $\|\nabla\bar{X} - (\nabla\bar{X})_s\|_1 \gg 1$ for many digital images, especially when the number of measurements is limited (so that s is small), taking a square root shall lead to a smaller bound than that without doing so.

Together with both scenarios, we can claim that if the level of noise τ is *relatively large* and *the number of measurements m is limited*, then the enhanced TV model (1.7) performs better than the TV model (1.2) in the sense of (3.20), because (3.20) is guaranteed to hold when

$$\sqrt{\frac{\sqrt{s}}{\alpha}}\tau + \sqrt{\frac{1}{\alpha}\|\nabla\bar{X} - (\nabla\bar{X})_s\|_1} \lesssim \frac{\|\nabla\bar{X} - (\nabla\bar{X})_s\|_1}{\sqrt{s}} + \tau,$$

and we can study $\sqrt{\frac{\sqrt{s}}{\alpha}}\tau \lesssim \tau$ and $\sqrt{\frac{1}{\alpha}\|\nabla\bar{X} - (\nabla\bar{X})_s\|_1} \lesssim \frac{\|\nabla\bar{X} - (\nabla\bar{X})_s\|_1}{\sqrt{s}}$ separately.

This comparison can be analogously extended to other cases for which the corresponding reconstruction error bounds are also linear with respect to terms $\|\nabla\bar{X} - (\nabla\bar{X})_s\|_1/\sqrt{s}$ and τ. Such examples include the model in [39], which has the regularization term $\|X\|_{\mathrm{TV}_a} - \|X\|_{\mathrm{TV}_i}$. For the model in [39], it seems that reconstruction guarantees leading to an error bound without

the log factor $\log(N^2/s)$ are still missing. Note that this log factor also occurs in the bound (1.9) for the TV model (1.2) and the bound (3.11) for the enhanced TV model (1.7), but it is removed if the required RIP order increases from $\mathcal{O}(s)$ to $\mathcal{O}(s\log^3(N))$, and then both bounds can be improved to (1.10) and (3.13), respectively. Reconstruction guarantees for the model in [39] have been investigated in [37]. However, the derived error bound (see theorem 3.8 in [37]) still fails to remove the log factor $\log(N^2/s)$, despite that the subsampled measurements are required to have the RIP of order $\mathcal{O}(s^2\log(N))$ with a more complicated level δ which depends on N, s, and the constant $\tilde{C}$ in lemma 2.1.

4. Proofs

In this section, we present the complete proofs for the theoretical results in section 3.

4.1. Proofs of proposition 3.1 and corollary 3.1

Proof of proposition 3.1. We arrange the indices in S^c in order of decreasing magnitudes (in absolute value) of D_{S^c} and divide S^c into subsets of size $4k\gamma^2$, i.e. $S^c = S_1 \bigcup S_2 \bigcup \cdots \bigcup S_r$, where $r = \left\lfloor \frac{N^2 - |S|}{4k\gamma^2} \right\rfloor$. In other words, $D_{S^c} = D_{S_1} + D_{S_2} + \cdots + D_{S_r}$, where D_{S_1} consists of the $4k\gamma^2$ largest-magnitude components of D over S^c, D_{S_2} consists of the next $4k\gamma^2$ largest-magnitude components of D over $S^c \backslash S_1$, and so forth. As the magnitude of each component of D_{S_j} is less than the average magnitude $\|D_{S_{j-1}}\|_1/(4k\gamma^2)$ of components of $D_{S_{j-1}}$, we have

$$\|D_{S_j}\|_2^2 \leqslant 4k\gamma^2 \left(\frac{\|D_{S_{j-1}}\|_1}{4k\gamma^2} \right)^2 = \frac{\|D_{S_{j-1}}\|_1^2}{4k\gamma^2}, \quad j = 2, 3, \ldots, r.$$

Thus, combining $\|D_{S_j}\|_2 \leqslant \frac{\|D_{S_{j-1}}\|_1}{2\gamma\sqrt{k}}$ with the cone constraint (3.2), we have

$$\sum_{j=2}^{r} \|D_{S_j}\|_2 \leqslant \frac{1}{2\gamma\sqrt{k}} \|D_{S^c}\|_1 \leqslant \frac{\|D_S\|_1}{2\sqrt{k}} - \frac{\beta_1}{4\gamma\sqrt{k}} \|D\|_2^2 + \frac{\sigma}{2\gamma\sqrt{k}} + \frac{\beta_2}{2\gamma\sqrt{k}} \langle E_1, E_2 \rangle.$$

The assumption $|S| \leqslant k$ leads to $\|D_S\|_1 \leqslant \sqrt{|S|}\|D_S\|_2 \leqslant \sqrt{k}\|D_S\|_2 \leqslant \sqrt{k}\|D_S + D_{S_1}\|_2$, hence we have

$$\sum_{j=2}^{r} \|D_{S_j}\|_2 \leqslant \frac{\|D_S + D_{S_1}\|_2}{2} - \frac{\beta_1}{4\gamma\sqrt{k}} \|D\|_2^2 + \frac{\sigma}{2\gamma\sqrt{k}} + \frac{\beta_2}{2\gamma\sqrt{k}} \langle E_1, E_2 \rangle. \tag{4.1}$$

Together with this bound (4.1), the tube constraint (3.1), and the RIP of $\mathcal{A}$, we have

$$\varepsilon \geqslant \|\mathcal{A}D\|_2 \geqslant \|\mathcal{A}(D_S + D_{S_1})\|_2 - \sum_{j=2}^{r} \|\mathcal{A}D_{S_j}\|_2$$

$$\geqslant \sqrt{1-\delta}\|D_S + D_{S_1}\|_2 - \sqrt{1+\delta}\sum_{j=2}^{r} \|D_{S_j}\|_2$$

$$\geqslant \sqrt{1-\delta}\|D_S + D_{S_1}\|_2 - \sqrt{1+\delta}\left(\frac{\|D_S + D_{S_1}\|_2}{2} - \frac{\beta_1\|D\|_2^2}{4\gamma\sqrt{k}} + \frac{\sigma}{2\gamma\sqrt{k}} + \frac{\beta_2}{2\gamma\sqrt{k}}\langle E_1, E_2 \rangle \right)$$

$$= \left(\sqrt{1-\delta} - \frac{\sqrt{1+\delta}}{2} \right) \|D_S + D_{S_1}\|_2 + \frac{\beta_1\sqrt{1+\delta}\|D\|_2^2}{4\gamma\sqrt{k}} - \frac{\sigma\sqrt{1+\delta}}{2\gamma\sqrt{k}} - \frac{\beta_2\sqrt{1+\delta}}{2\gamma\sqrt{k}}\langle E_1, E_2 \rangle.$$

The assumption $\delta < 0.6$ ensures $\sqrt{1-\delta} - \sqrt{1+\delta}/2 > 0$. Hence, we have

$$\|D_S + D_{S_1}\|_2 \leqslant \frac{2}{2\sqrt{1-\delta} - \sqrt{1+\delta}} \left(\varepsilon - \frac{\beta_1 \sqrt{1+\delta}\|D\|_2^2}{4\gamma\sqrt{k}} + \frac{\sigma\sqrt{1+\delta}}{2\gamma\sqrt{k}} + \frac{\beta_2\sqrt{1+\delta}}{2\gamma\sqrt{k}}\langle E_1, E_2\rangle \right).$$

As $\|D\|_2$ is bounded by the sum of $\|D_S + D_{S_1}\|_2$ and $\sum_{j=2}^r \|D_{S_j}\|_2$, it satisfies

$$\|D\|_2 \leqslant \frac{3}{2}\|D_S + D_{S_1}\|_2 - \frac{\beta_1}{4\gamma\sqrt{k}}\|D\|_2^2 + \frac{\sigma}{2\gamma\sqrt{k}} + \frac{\beta_2}{2\gamma\sqrt{k}}\langle E_1, E_2\rangle$$

$$\leqslant \frac{3}{2\sqrt{1-\delta} - \sqrt{1+\delta}}\varepsilon + \left(\frac{3}{2\sqrt{1-\delta} - \sqrt{1+\delta}} + \frac{1}{\sqrt{1+\delta}} \right) \cdot$$

$$\left(-\frac{\beta_1\sqrt{1+\delta}}{4\gamma\sqrt{k}}\|D\|_2^2 + \frac{\sqrt{1+\delta}}{2\gamma\sqrt{k}}\sigma + \frac{\beta_2\sqrt{1+\delta}}{2\gamma\sqrt{k}}\langle E_1, E_2\rangle \right)$$

$$:= K_1\varepsilon - \frac{\beta_1 K_2}{\gamma\sqrt{k}}\|D\|_2^2 + \frac{2K_2}{\gamma\sqrt{k}}\sigma + \frac{2\beta_2 K_2}{\gamma\sqrt{k}}\langle E_1, E_2\rangle.$$

Thus, we have the quadratic inequality

$$\frac{\beta_1 K_2}{\gamma\sqrt{k}}\|D\|_2^2 + \|D\|_2 - \frac{2\beta_2 K_2}{\gamma\sqrt{k}}\langle E_1, E_2\rangle - K_1\varepsilon - \frac{2K_2}{\gamma\sqrt{k}}\sigma \leqslant 0. \tag{4.2}$$

The requirement (3.3) on β_2 ensures that

$$\|D\|_2 - \frac{2\beta_2 K_2}{\gamma\sqrt{k}}\langle E_1, E_2\rangle \geqslant \|D\|_2 - \left\langle \frac{E_1}{\|E_1\|_2}, E_2 \right\rangle \geqslant 0,$$

where the last inequality is due to Cauchy–Schwarz inequality and $\|E_2\|_2 = \|D\|_2$. Then, we have

$$\frac{\beta_1 K_2}{\gamma\sqrt{k}}\|D\|_2^2 - K_1\varepsilon - \frac{2K_2}{\gamma\sqrt{k}}\sigma \leqslant 0,$$

which yields the estimation (3.4). Finally, we derive (3.5). As $|S| \leqslant k$, we have $\|D_S\|_1 \leqslant \sqrt{k}\|D_S\|_2$. Then, together with the requirement (3.3) on β_2 and the cone constraint (3.2), we have

$$\|D\|_1 \leqslant (\gamma+1)\|D_S\|_1 - \frac{\beta_1}{2}\|D\|_2^2 + \sigma + \beta_2\langle E_1, E_2\rangle \leqslant (\gamma+1)\|D_S\|_1 + \sigma + \frac{\gamma\sqrt{k}}{2K_2}\|D\|_2$$

$$\leqslant (\gamma+1)\sqrt{k}\|D_S\|_2 + \sigma + \frac{\gamma\sqrt{k}}{2K_2}\|D\|_2 \leqslant (\gamma+1)\sqrt{k}\|D\|_2 + \sigma + \frac{\gamma\sqrt{k}}{2K_2}\|D\|_2 \tag{4.3}$$

$$= \frac{(2K_2+1)\gamma\sqrt{k} + 2K_2\sqrt{k}}{2K_2}\|D\|_2 + \sigma,$$

which completes the proof of proposition 3.1. $\qquad\square$

Proof of corollary 3.1. In the second inequality of (4.3), we use the fact $-\frac{\beta_1}{2}\|D\|_2^2 \leqslant 0$. If $\|D\|_2$ satisfies $\|D\|_2 \geqslant \sqrt{2\sigma/\beta_1}$, then $-\frac{\beta_1}{2}\|D\|_2^2 + \sigma \leqslant 0$ and it follows from (4.3) that

$$\|D\|_1 \leqslant (\gamma+1)\|D_S\|_1 - \frac{\beta_1}{2}\|D\|_2^2 + \sigma + \beta_2\langle E_1, E_2\rangle$$

$$\leqslant (\gamma+1)\|D_S\|_1 + \frac{\gamma\sqrt{k}}{2K_2}\|D\|_2 \leqslant \frac{(2K_2+1)\gamma\sqrt{k} + 2K_2\sqrt{k}}{2K_2}\|D\|_2,$$

which completes the proof of corollary 3.1. $\qquad\square$

4.2. Proof of theorem 3.1 and corollary 3.2

We first prove the stable gradient reconstruction results (3.9) and (3.10), and then obtain the stable image reconstruction result (3.11) with the aid of a strong Sobolev inequality. The following Sobolev inequality was derived in [47] for images with multivariate generalization given in [46].

Lemma 4.1 (strong Sobolev inequality). *Let* $\mathcal{B} : \mathbb{C}^{N \times N} \to \mathbb{C}^m$ *be a linear map such that* $\mathcal{B}\mathcal{H}^* : \mathbb{C}^{N \times N} \to \mathbb{C}^m$ *has the RIP of order* $2s + 1$ *and level* $\delta < 1$, *where* $\mathcal{H} : \mathbb{C}^{N \times N} \to \mathbb{C}^{N \times N}$ *is the bivariate Haar transform. Suppose that* $D \in \mathbb{C}^{N \times N}$ *satisfies the tube constraint* $\|\mathcal{B}D\|_2 \leqslant \varepsilon$. *Then*

$$\|D\|_2 \leqslant C_2 \left[\left(\frac{\|\nabla D\|_1}{\sqrt{s}} \right) \log \left(\frac{N^2}{s} \right) + \varepsilon \right].$$

Proof of theorem 3.1. The proof is divided into the stable gradient and image reconstructions, respectively.

Stable gradient reconstruction. We plan to apply proposition 3.1 to the term $\nabla(X^{\mathrm{opt}} - \bar{X})$. Let $V = X^{\mathrm{opt}} - \bar{X}$ and $L = (V_x, V_y^{\mathrm{T}})$. For convenience, let P denote the mapping of indices which maps the index of a nonzero entry in ∇V to its corresponding index in L. By the definition of ∇, L has the same norm as ∇V, i.e. $\|L\|_2 = \|\nabla V\|_2$ and $\|L\|_1 = \|\nabla V\|_1$. Thus, it suffices to apply proposition 3.1 to L. Let $A_1, A_2, \ldots, A_{m_1}, A'_1, A'_2, \ldots, A'_{m_1}$ be such that $[\mathcal{A}(Z)]_j = \langle A_j, Z \rangle$ and $[\mathcal{A}'(Z)]_j = \langle A'_j, Z \rangle$.

- *Cone constraint.* Let S denote the support of the largest s entries of $\nabla \bar{X}$. On one hand, it holds that

$$\|\nabla X^{\mathrm{opt}}\|_1 - \frac{\alpha}{2} \|\nabla X^{\mathrm{opt}}\|_2^2 \leqslant \|\nabla \bar{X}\|_1 - \frac{\alpha}{2} \|\nabla \bar{X}\|_2^2$$
$$= \|(\nabla \bar{X})_S\|_1 + \|(\nabla \bar{X})_{S^c}\|_1 - \frac{\alpha}{2} \|\nabla \bar{X}\|_2^2.$$

On the other hand, we have

$$\|\nabla X^{\mathrm{opt}}\|_1 - \frac{\alpha}{2} \|\nabla X^{\mathrm{opt}}\|_2^2$$
$$= \|(\nabla \bar{X})_S + (\nabla V)_S\|_1 + \|(\nabla \bar{X})_{S^c} + (\nabla V)_{S^c}\|_1 - \frac{\alpha}{2} \|\nabla \bar{X} + \nabla V\|_2^2$$
$$\geqslant \|(\nabla \bar{X})_S\|_1 - \|(\nabla V)_S\|_1 + \|(\nabla V)_{S^c}\|_1 - \|(\nabla \bar{X})_{S^c}\|_1$$
$$- \frac{\alpha}{2} \left(\|\nabla \bar{X}\|_2^2 + 2\langle \nabla \bar{X}, \nabla V \rangle + \|\nabla V\|_2^2 \right).$$

Thus, we obtain

$$\|(\nabla V)_{S^c}\|_1 \leqslant \|(\nabla V)_S\|_1 + 2\|(\nabla \bar{X})_{S^c}\|_1 + \frac{\alpha}{2} \|\nabla V\|_2^2 + \alpha\langle \nabla \bar{X}, \nabla V \rangle$$
$$= \|(\nabla V)_S\|_1 + 2\|\nabla \bar{X} - (\nabla \bar{X})_s\|_1 - \frac{\alpha}{2} \|\nabla V\|_2^2 + \alpha\langle \nabla X^{\mathrm{opt}}, \nabla V \rangle.$$

As L contains all the same nonzero entries as ∇V, it satisfies the following cone constraint:

$$\|L_{P(S)^c}\|_1 \leqslant \|L_{P(S)}\|_1 + 2\|\nabla \bar{X} - (\nabla \bar{X})_s\|_1 - \frac{\alpha}{2} \|L\|_2^2 + \alpha\langle \nabla X^{\mathrm{opt}}, \nabla V \rangle.$$

- *Tube constraint.* We note that V satisfies a tube constraint as

$$\|\mathcal{M}V\|_2^2 = \|(\mathcal{M}X^{\mathrm{opt}} - y) - (\mathcal{M}\bar{X} - y)\|_2^2 \leqslant 2\|\mathcal{M}X^{\mathrm{opt}} - y\|_2^2 + 2\|\mathcal{M}\bar{X} - y\|_2^2 \leqslant 4\tau^2.$$

Then, it follows from lemma 3.1 that

$$|\langle A_j, V_x \rangle|^2 = |\langle [A_j]^0, V \rangle - \langle [A_j]_0, V \rangle|^2 \leqslant 2|\langle [A_j]^0, V \rangle|^2 + 2|\langle [A_j]_0, V \rangle|^2$$

and

$$|\langle A_j', V_y^{\mathrm{T}} \rangle|^2 = |\langle [A_j']^0, V^{\mathrm{T}} \rangle - \langle [A_j']_0, V^{\mathrm{T}} \rangle|^2 \leqslant 2|\langle [A_j']^0, V^{\mathrm{T}} \rangle|^2 + 2|\langle [A_j']_0, V^{\mathrm{T}} \rangle|^2.$$

Thus, L also satisfies a tube constraint:

$$\|[\mathcal{A}\ \mathcal{A}']L\|_2^2 = \sum_{j=1}^{m} |\langle A_j, V_x \rangle|^2 + |\langle A_j', V_y^{\mathrm{T}} \rangle|^2 \leqslant 2\|\mathcal{M}(V)\|_2^2 \leqslant 8\tau^2.$$

By virtue of proposition 3.1 with $\gamma = 1$, $k = s$, $\beta_1 = \beta_2 = \alpha$, $\sigma = 2\|\nabla \bar{X} - (\nabla \bar{X})_s\|_1$, $\varepsilon = 2\sqrt{2}\tau$, $E_1 = \nabla X^{\mathrm{opt}}$ and $E_2 = \nabla V$, the requirement (3.8) of α ensures that

$$\|\nabla X^{\mathrm{opt}} - \nabla \bar{X}\|_2 = \|L\|_2 \leqslant \sqrt{\frac{2\sqrt{2}\sqrt{s}K_1}{\alpha K_2}\tau + \frac{4}{\alpha}\|\nabla X - (\nabla X)_s\|_1}.$$

Furthermore, by (3.5), we have $\|\nabla X^{\mathrm{opt}} - \nabla \bar{X}\|_1 = \|L\|_1$ and

$$\|L\|_1 \leqslant \frac{(4K_2 + 1)\sqrt{s}}{2K_2}\sqrt{\frac{2\sqrt{2}\sqrt{s}K_1}{\alpha K_2}\tau + \frac{4}{\alpha}\|\nabla \bar{X} - (\nabla \bar{X})_s\|_1} + 2\|\nabla \bar{X} - (\nabla \bar{X})_s\|_1, \qquad (4.4)$$

which completes the proof of the stable gradient reconstruction results (3.9) and (3.10).

Stable image reconstruction. We now apply the strong Sobolev inequality given in lemma 4.1 to $X^{\mathrm{opt}} - \bar{X}$. As $\|\mathcal{B}(X^{\mathrm{opt}} - \bar{X})\|_2 \leqslant \|\mathcal{M}(X^{\mathrm{opt}} - \bar{X})\|_2 \leqslant 2\tau$, we have

$$\|X^{\mathrm{opt}} - \bar{X}\|_2 \lesssim \log\left(\frac{N^2}{s}\right)\left(\frac{\|\nabla X^{\mathrm{opt}} - \nabla \bar{X}\|_1}{\sqrt{s}}\right) + \tau.$$

Together with the bound (3.10), we have the stable image reconstruction result (3.11). $\qquad \square$

Proof of corollary 3.2. If $\|\nabla \bar{X} - \nabla X^{\mathrm{opt}}\|_2 \geqslant \sqrt{\frac{2}{\alpha}}\|\nabla \bar{X} - (\nabla \bar{X})_s\|_1$, then it follows from corollary 3.1 that the linear term of $\|\nabla \bar{X} - (\nabla \bar{X})_s\|_1$ in the estimation (4.4) can be removed. Thus, from (4.4) to (3.11), the term $\log(\frac{N^2}{s})\frac{\|\nabla \bar{X} - (\nabla \bar{X})_s\|_1}{\sqrt{s}}$ in (3.11) can be also removed. $\qquad \square$

4.3. Proof of theorem 3.2

We apply proposition 3.1 to $c = \mathcal{H}V$ as opposed to ∇V. Some properties of the bivariate Haar wavelet system, characterized as lemmas 2.1, 2.2, and 2.2, are needed in the proof. Besides, a classical Sobolev inequality weaker than the strong Sobolev inequality in lemma 4.1 is needed.

Lemma 4.2 ([47]). *Let $X \in \mathbb{C}^{N \times N}$ be a mean-zero image or contain some zero-valued pixels. Then*

$$\|X\|_2 \leqslant \|\nabla X\|_1. \qquad (4.5)$$

Proof of theorem 3.2. Let $V = X^{\mathrm{opt}} - \bar{X}$, and apply proposition 3.1 to $c = \mathcal{H}V$, where $c_{(1)} := c_{(1)}(V)$ denotes the Haar coefficient corresponding to the constant wavelet, and $c_{(j)} := c_{(j)}(V)$ ($j \geqslant 2$) denotes the $(j-1)$-st largest-magnitude Haar coefficient among the remaining. We use this ordering because lemma 2.1 applies only to mean-zero images. Let $h_{(j)}$ denote the Haar

wavelet associated with $c_{(j)}$. We have assumed that the composite operator $\mathcal{M}\mathcal{H}^* : \mathbb{C}^{N \times N} \to \mathbb{C}^m$ has the RIP of order $Cs \log^3(N)$ and level $\delta < 0.6$, and we now derive the constant C.

- *Cone constraint on $c = \mathcal{H}V$.* As shown in section 4.2, we have

$$\|(\nabla V)_{S^c}\|_1 \leqslant \|(\nabla V)_S\|_1 + 2\|\nabla \bar{X} - (\nabla \bar{X})_s\|_1 - \frac{\alpha}{2}\|\nabla V\|_2^2 + \alpha \langle \nabla X^{\text{opt}}, \nabla V \rangle. \tag{4.6}$$

Recall that S is the index set of s largest-magnitude entries of ∇V. It follows from lemma 2.2 that the set Ω of wavelets which are non-constant over S has the cardinality at most $6s \log(N)$, i.e. $|\Omega| \leqslant 6s \log(N)$. Decompose V as

$$V = \sum_j c_{(j)} h_{(j)} = \sum_{j \in \Omega} c_{(j)} h_{(j)} + \sum_{j \in \Omega^c} c_{(j)} h_{(j)} =: V_\Omega + V_{\Omega^c}.$$

Because of the linearity of ∇, we have $\nabla V = \nabla V_\Omega + \nabla V_{\Omega^c}$. By the construction of Ω, we have $(\nabla V_{\Omega^c})_S = 0$, which leads to $(\nabla V)_S = (\nabla V_\Omega)_S$. Then, it follows from lemma 2.3 that

$$\|(\nabla V)_S\|_1 = \|(\nabla V_\Omega)_S\|_1 \leqslant \|\nabla V_\Omega\|_1 \leqslant \sum_{j \in \Omega} |c_{(j)}| \|\nabla h_{(j)}\|_1 \leqslant 8 \sum_{j \in \Omega} |c_{(j)}|.$$

Let $k = 6s \log(N)$, $\|c_\Omega\|_1$ and $\|c_{\Omega^c}\|_1$ denote $\sum_{j \in \Omega} |c_{(j)}|$ and $\sum_{j \in \Omega^c} |c_{(j)}|$, respectively. Concerning the decay of the wavelet coefficients in lemma 2.1, we have $|c_{(j+1)}| \leqslant \tilde{C} \|\nabla V\|_1 / j$. Together with the cone constraint (4.6) for ∇V, we have

$$\|c_{\Omega^c}\|_1 \leqslant \sum_{j=s+1}^{N^2} |c_{(j)}| \leqslant \tilde{C} \sum_{j=s+1}^{N^2} \frac{\|\nabla V\|_1}{j-1} \overset{(\diamond)}{\leqslant} C' \log\left(\frac{N^2}{s}\right)$$

$$\leqslant C' \log\left(\frac{N^2}{s}\right) \left(2\|(\nabla V)_S\|_1 + 2\|\nabla \bar{X} - (\nabla \bar{X})_s\|_1 - \frac{\alpha}{2}\|\nabla V\|_2^2 + \alpha \langle \nabla X^{\text{opt}}, \nabla V \rangle\right)$$

$$\leqslant C' \log\left(\frac{N^2}{s}\right) \left(16\|c_\Omega\|_1 + 2\|\nabla \bar{X} - (\nabla \bar{X})_s\|_1 - \frac{\alpha}{2}\|\nabla V\|_2^2 + \alpha \|\nabla X^{\text{opt}}\|_2 \|\nabla\|_2 \|V\|_2\right)$$

$$\overset{(*)}{\leqslant} C' \log\left(\frac{N^2}{s}\right) \left(16\|c_\Omega\|_1 + 2\|\nabla \bar{X} - (\nabla \bar{X})_s\|_1 - \frac{\alpha}{2}\|\nabla V\|_2^2 + \alpha\sqrt{8} \|\nabla X^{\text{opt}}\|_2 \|V\|_2\right),$$

where $(\diamond)$ is due to the property of partial sum of harmonic series [22], and $(*)$ is due to the fact $\|\nabla\|_2^2 \leqslant 8$ [13]. As we prepare to apply proposition 3.1 to $c = \mathcal{H}V$, we need to bound $\|\nabla V\|_2$ below in terms of $\|V\|_2 = \|c\|_2$, where $\|V\|_2 = \|c\|_2$ is due to Parseval's identity and the fact that $\{h_{(j)}\}$ forms an orthonormal basis for $\mathbb{C}^{N \times N}$. As $\|\nabla V\|_2 \geqslant \frac{1}{\sqrt{2N}}\|\nabla V\|_1$, the classical Sobolev inequality (4.5) implies

$$\|\nabla V\|_2 \geqslant \frac{1}{\sqrt{2N}}\|V\|_2. \tag{4.7}$$

Thus we have

$$\|c_{\Omega^c}\|_1 \leqslant C' \log\left(\frac{N^2}{s}\right) \left(16\|c_\Omega\|_1 + 2\|\nabla \bar{X} - (\nabla \bar{X})_s\|_1 - \frac{\alpha\|c\|_2^2}{4N^2}\right.$$
$$\left. + \alpha\sqrt{8}\|\nabla X^{\text{opt}}\|_2 \|c\|_2\right). \tag{4.8}$$

- *Tube constraint* $\|\mathcal{M}\mathcal{H}^*c\|_2 \leqslant 2\tau$. As $\bar{X}$ and X^{opt} are in the feasible region of the model (1.7), for $c = \mathcal{H}V = \mathcal{H}X^{\mathrm{opt}} - \mathcal{H}\bar{X}$, we have

$$\|\mathcal{M}\mathcal{H}^*c\|_2 = \|\mathcal{M}X^{\mathrm{opt}} - \mathcal{M}\bar{X}\|_2 \leqslant \|\mathcal{M}X^{\mathrm{opt}} - y\|_2 + \|\mathcal{M}\bar{X} - y\|_2 \leqslant 2\tau.$$

Under the derived cone and tube constraints on c, along with the RIP condition on $\mathcal{M}\mathcal{H}^*$, theorem 3.2 is proved by applying proposition 3.1 and using $\gamma = 16C'\log(N^2/s) \leqslant 32C'\log(N)$, $k = 6s\log(N)$, $\sigma = 2C'\log(N^2/s)\|\nabla\bar{X} - (\nabla\bar{X})_s\|_1$, $E_1 = \sqrt{8}\|\nabla X^{\mathrm{opt}}\|_2$, $E_2 = \|c\|_2$, $\beta_1 = \alpha C'\log(N^2/s)/(2N^2)$, and $\beta_2 = \alpha C'\log(N^2/s)$. In fact, $5k\gamma^2$ with both particular k and γ leads to the required RIP order $Cs\log^3(N)$ for $\mathcal{M}\mathcal{H}^*$. Together with all these factors and proposition 3.1, we know that if

$$\alpha \leqslant \frac{\sqrt{8}\sqrt{6s\log(N)}}{K_2\|\nabla X^{\mathrm{opt}}\|_2},$$

then it holds that

$$\|V\|_2 = \|c\|_2 \leqslant \sqrt{\frac{64N^2\sqrt{6s\log(N)}K_1}{\alpha K_2}\tau + \frac{8N^2}{\alpha}\|\nabla\bar{X} - (\nabla\bar{X})_s\|_1},$$

which leads to the estimation (3.13).   □

4.4. Proof of theorem 3.3

The proof of theorem 3.3 follows the approach of theorem 3.2, in which the *local coherence* of the sensing basis (Fourier) with respect to the sparsity basis (Haar wavelet) plays a major role.

Definition 4.1 (local coherence [36]). The *local coherence* of an orthonormal basis $\Phi = \{\phi_j\}_{j=1}^N$ of $\mathbb{C}^N$ with respect to the orthonormal basis $\Psi = \{\psi_k\}_{k=1}^N$ of $\mathbb{C}^N$ is the function $\mu^{\mathrm{loc}}(\Phi,\Psi) \in \mathbb{R}^N$ defined coordinate-wise by

$$\mu_j^{\mathrm{loc}}(\Phi,\Psi) = \sup_{1\leqslant k\leqslant N}|\langle\phi_j,\psi_k\rangle|, \quad j = 1,2,\ldots,N.$$

The following result indicates that, with high probabilities, signals can be stably reconstructed from subsampled measurements with the local coherence function appropriately used. It can be deemed as a finite-dimensional analog to [53, theorem 2.1], and a proof can be found in [36].

Lemma 4.3. *Let* $\Phi = \{\phi_j\}_{j=1}^N$ *and* $\Psi = \{\psi_k\}_{k=1}^N$ *be two orthonormal bases of* $\mathbb{C}^N$. *Assume the local coherence of* Φ *with respect to* Ψ *is point-wise bounded by the function* κ *in the sense of*

$$\sup_{1\leqslant k\leqslant N}|\langle\phi_j,\psi_k\rangle| \leqslant \kappa_j.$$

Fix $\delta > 0$ *and integers* N, m, *and* s *such that* $s \gtrsim \log(N)$ *and* $m \gtrsim \delta^{-2}\|\kappa\|_2^2 s\log^3(s)\log(N)$, *and choose* m *(possibly not distinct) indices* $j \in \Omega \subset \{1,2,\ldots,N\}$ *i.i.d. from the probability measure* ν *on* $\{1,2,\ldots,N\}$ *given by* $v(j) = \kappa_j^2/\|\kappa\|_2^2$.

Consider the matrix $A \in \mathbb{C}^{m\times N}$ *with entries* $A_{j,k} = \langle\phi_j,\psi_k\rangle$, $j \in \Omega$, $k \in \{1,2,\ldots,N\}$, *and consider the diagonal matrix* $G = \mathrm{diag}(g) \in \mathbb{C}^{m\times m}$ *with* $g_j = \|\kappa\|_2/\kappa_j, j = 1,\ldots,m$. *Then with probability at least* $1 - N^{-c\log^3(s)}$, *the RIC* δ_s *of the preconditioned matrix* $\frac{1}{\sqrt{m}}GA$ *satisfies* $\delta_s \leqslant \delta$.

In particular, the following result describes the local coherence of the orthonormal Fourier basis with respect to the orthonormal Haar wavelet basis, which was initially occurred in [36].

Lemma 4.4 (theorem 4 in [36], slightly modified). *Let $N = 2^n$ be a power of 2, where $n \in \mathbb{N}^+$. The local coherence μ^{loc} of the orthonormal two-dimensional Fourier basis $\{\varphi_{k_1,k_2}\}$ with respect to the orthonormal bivariate Haar wavelet basis $\{h^\ell_{j,k}\}$ in $\mathbb{C}^{N \times N}$ is bounded by*

$$\mu^{\mathrm{loc}}_{k_1,k_2} \leqslant \kappa(k_1,k_2) := \min\left(1, \frac{18\pi}{\max(|k_1|,|k_2|)}\right) \kappa'(k_1,k_2) := \min\left(1, \frac{18\pi\sqrt{2}}{(|k_1|^2 + |k_2|^2)^{1/2}}\right),$$

and one has $\|\kappa\|_2 \leqslant \|\kappa'\|_2 \leqslant \sqrt{17\,200 + 502\log(N)}$.

Remark 4.1. For theorem 4 in [36], $n \geqslant 8$ was assumed to ensure $17200 + 502\log(N) \leqslant 2700\log(N)$ and hence $\|\kappa\|_2 \leqslant \|\kappa'\|_2 \leqslant 52\sqrt{\log(N)}$. We regard the assumption as a restriction on the size $N \times N$ of images, thus we remove this assumption and adopt the bound $\sqrt{17200 + 502\log N}$ in our following proof. Besides, it was conjectured in [36] that the factor 2700 is due to lack of smoothness for the Haar wavelets, and this factor might be removed by considering smoother wavelets.

Proof of theorem 3.3. Let $P \in \mathbb{C}^{m \times m}$ be the diagonal matrix encoding the weights in the noise model. That is, $P = \mathrm{diag}(\rho)$, where, for κ' as in lemma 4.4, $\rho \in \mathbb{C}^m$ is a vector converted from the matrix

$$\rho(k_1,k_2) = \frac{\|\kappa'\|_2}{\kappa'(k_1,k_2)} = C\sqrt{1 + \log(N)}\max\left(1, \frac{(|k_1|^2 + |k_2|^2)^{1/2}}{18\pi}\right), \quad (k_1,k_2) \in \Omega.$$

Note that $Pg = \rho \circ g$ for $g \in \mathbb{C}^m$. Together with the particular incoherence estimate in lemma 4.4, lemma 4.3 implies that with probability at least $1 - N^{-2c\log^3(s)}$ (as c is a generic constant, the factor 2 of c is removed in the statement of theorem 3.3), $\mathcal{A} := \frac{1}{\sqrt{m}} P \mathcal{F}_\Omega \mathcal{H}^*$ has the RIP of order s and level $\delta < 0.6$ once $s \gtrsim \log(N^2) \gtrsim \log(N)$ and

$$m \gtrsim s\delta^{-2}\log^3(s)\log^2(N^2) \gtrsim s\delta^{-2}\log^3(s)\log^2(N).$$

By the assumption $m \gtrsim s\log^3(s)\log^5(N)$ (in fact, we shall assume $m \gtrsim s\delta^{-2}\log^3(s)\log^5(N)$), we can assume that $\mathcal{A}$ has the RIP of order $\bar{s} = Cs\log^3(N)$ and level $\delta < 0.6$, where C is the constant derived in theorem 3.2. Moreover, let $V = X^{\mathrm{opt}} - \bar{X}$ and apply proposition 3.1 again to $c = \mathcal{H}V$, where $c_{(1)} := c_{(1)}(V)$ denotes the Haar coefficient corresponding to the constant wavelet, and $c_{(j)} := c_{(j)}(V)$ ($j \geqslant 2$) denotes the $(j-1)$st largest-magnitude Haar coefficient among the remaining. To apply proposition 3.1, we need to find cone and tube constraints for $c = \mathcal{H}V$.

- *Cone constraint on $c = \mathcal{H}V$,* which is the same as (4.8) in the proof of theorem 3.2.
- *Tube constraint $\|\mathcal{A}c\|_2 = \|\mathcal{A}\mathcal{H}V\|_2 \leqslant \sqrt{2}\tau$,* since

$$\begin{aligned}
m\|\mathcal{A}\mathcal{H}V\|_2^2 &= \|P\mathcal{F}_\Omega\mathcal{H}^*\mathcal{H}V\|_2^2 = \|\rho \circ (\mathcal{F}_\Omega V)\|_2^2 \\
&\leqslant \|\rho \circ (\mathcal{F}_\Omega X^{\mathrm{opt}} - b)\|_2^2 + \|\rho \circ (\mathcal{F}_\Omega \bar{X} - b)\|_2^2 \leqslant 2m\tau^2.
\end{aligned}$$

The rest is similar to the proof of theorem 3.2, and the only trivial difference is the tube constraint, where 2τ there is replaced by $\sqrt{2}\tau$ here. Hence, we omit the following steps, and the estimation for the setting in this theorem, with constants removed, is the same as (3.13). $\qquad\square$
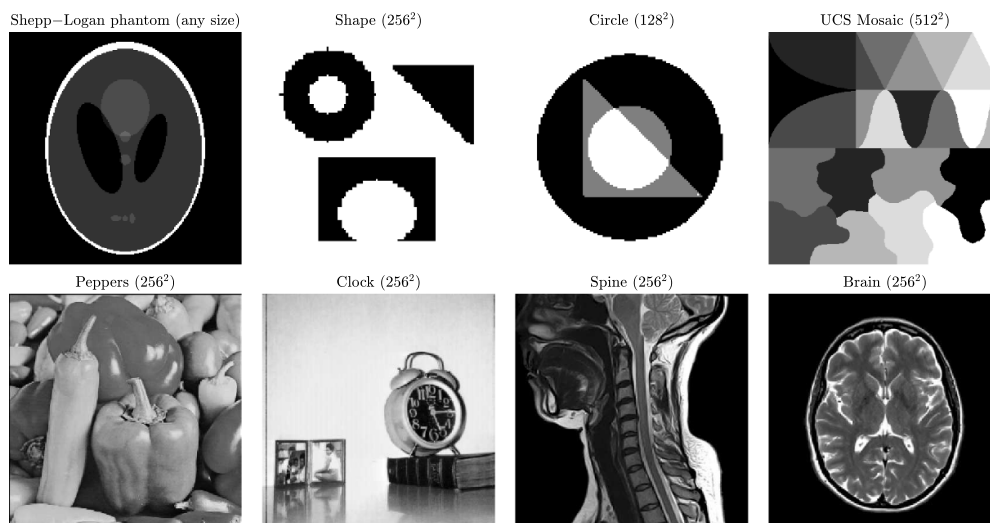
Figure 4. Test images.

5. Numerical experiments

We now report some experimental results to validate the effectiveness and numerical solvability of the enhanced TV model (1.7). As previously mentioned, the model (1.7) is of difference-of-convex, and it can be solved by some well-developed algorithms in the literature. We include the details of an algorithm in appendix C. For comparison, we consider the TV model (1.2) and the $TV_a - TV_i$ model in [39]. In our experiments, the TV model (1.2) is solved by the split Bregman method studied in [32], and the $TV_a - TV_i$ model is solved by the difference-of-convex functions algorithm (DCA) with subproblems solved by the split Bregman method in [39]. Details of the tuned parameters of these algorithms are stated in appendix C.

As displayed in figure 4, we test the standard *Shepp–Logan phantom*, three more synthetic piecewise-constant images (*Shape*, *Circle*, and *USC Mosaic*), two natural images (*Pepper* and *Clock*), and two medical images (*Spine* and *Brain*). Two sampling strategies are considered in our experiments. The first one is the *radial lines* sampling, and the other one is the strategy (3.15) proposed in theorem 3.3, which is referred to as the *MRI-desired* sampling strategy below. All codes were written by MATLAB R2021b, and all numerical experiments were conducted on a laptop (16 GB RAM, Intel CoreTM i7-9750H Processor) with macOS Monterey 12.1.

Example #1: Shepp–Logan phantom. The Shepp–Logan phantom is a standard image in the field of image reconstruction. Our experiments for this image are organized into three parts. The first part concentrates on the reconstruction of the Shepp–Logan phantom of size 256×256 from noise-free measurements, and α is fixed as 0.8 in the enhanced TV model (1.7). We sample along 15, 8, and 7 radial lines, corresponding to sampling rates 6.44%, 3.98%, and 3.03%, respectively. We also take MRI-desired measurements with rates 2.29%, 1.91%, and 1.53%. As shown in figure 5, the enhanced TV model (1.7) produces accurate reconstruction in all six sampling settings, and reconstruction quality is much better than those in comparison when the amount of samples is limited (e.g. 7 radial lines and 1.53% MRI-desired measurements). This observation confirms the result presented in section 3.3, which state that the reconstruction error bound (3.18) for the enhanced TV model (1.7) is tighter than (1.10)
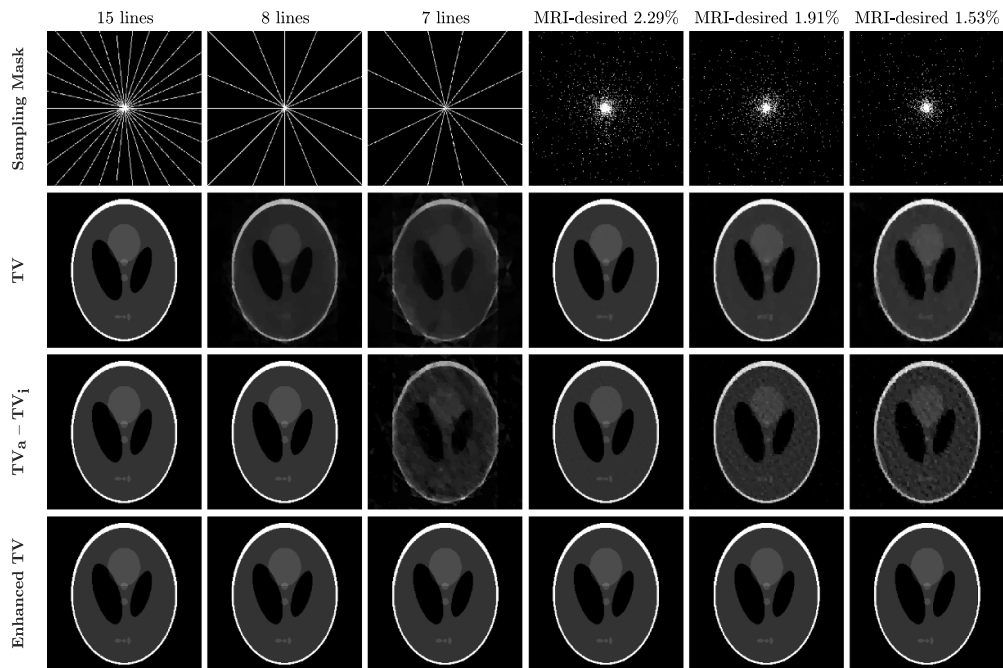
Figure 5. Shepp–Logan phantom: comparison of three models with radial line-sampled and MRI-desired measurements.

for the TV model (1.7) with a limited amount of noise-free measurements. As mentioned in section 3.3, such a result also pertains to the comparison between the enhanced TV model (1.7) and the $TV_a - TV_i$ model in [39].

Table 1 presents the relative errors in the Frobenius sense and the structural similarity index measure (SSIM) values in the format of 'relative error (SSIM value)' for comparison, in which the least error in each setting is printed in bold. The advantages of the enhanced TV model (1.7) become apparent when the available measurements are limited (e.g. when the sampling rate is below 3.03%). However, when measurements are relatively sufficient, as in the cases of 15 lines and 8 lines, the enhanced TV model (1.7) does not produce the least error reconstruction. Notably, though the outperformance of the enhanced TV model (1.7) is not sustained as measurements become sufficient, the difference of three models is too tiny to be visually observed. Furthermore, it is worth noting that the SSIM values are 1.0000 for the enhanced TV model (1.7) in all six sampling settings, indicating that this model's stability with respect to the number of measurements is well illustrated for the Shepp–Logan phantom image. We also report the performance of the enhanced isotropic TV model (labeled as 'Enhanced TV-isotropic' in table 1), using the algorithm described in appendix C. However, we observe that the enhanced isotropic TV model does not perform better than the enhanced anisotropic TV model (1.7), and it even fails for the case of 7 lines, reporting 8.794×10^{13} (0.0000) and implying that $\alpha = 0.8$ is severely large for it. If $\alpha = 0.6$ for the enhanced isotropic TV model, then 0.3970 (0.6288) is reported for the case of 7 lines. This observation can be partially explained

Table 1. Relative errors and SSIM values of the reconstructed images in figure 5 and images reconstructed using the enhanced isotropic TV regularization.

	TV	$TV_a - TV_i$	Enhanced TV	Enhanced TV-isotropic
15 lines (6.44%)	1.924×10^{-13} (1.0000)	$\mathbf{7.845 \times 10^{-14}}$ (1.0000)	2.977×10^{-12} (1.0000)	1.212×10^{-7} (1.0000)
8 lines (3.98%)	0.2456 (0.6764)	$\mathbf{3.852 \times 10^{-9}}$ (1.0000)	7.841×10^{-7} (1.0000)	1.233×10^{-3} (1.0000)
7 lines (3.03%)	0.4819 (0.4612)	0.3968 (0.5209)	$\mathbf{1.608 \times 10^{-6}}$ (1.0000)	/
MRI-desired (2.29%)	0.0415 (0.9890)	0.0266 (0.9896)	$\mathbf{8.069 \times 10^{-6}}$ (1.0000)	8.069×10^{-3} (0.9994)
MRI-desired (1.91%)	0.1575 (0.8937)	0.1837 (0.8404)	$\mathbf{2.324 \times 10^{-5}}$ (1.0000)	1.017×10^{-2} (0.9990)
MRI-desired (1.53%)	0.2826 (0.7473)	0.2983 (0.7374)	$\mathbf{8.456 \times 10^{-5}}$ (1.0000)	1.584×10^{-2} (0.9978)

Table 2. Relative errors and SSIM values of the reconstructed images in figure 5, with three levels of noise std = 0.04, 0.06, and 0.08.

	TV	$TV_a - TV_i$	Enhanced TV
15 lines (6.44%), std = 0.04	0.1796 (0.5759)	0.1860 (0.4534)	**0.0921** (0.9531)
15 lines (6.44%), std = 0.06	0.2506 (0.4866)	0.2748 (0.3161)	**0.1038** (0.9490)
15 lines (6.44%), std = 0.08	0.3111 (0.4265)	0.3535 (0.2448)	**0.1496** (0.9359)
MRI-desired (6.50%), std = 0.04	0.1041 (0.7322)	0.1376 (0.5721)	**0.0873** (0.9588)
MRI-desired (6.50%), std = 0.06	0.1498 (0.6101)	0.2082 (0.4179)	**0.1393** (0.9477)
MRI-desired (6.50%), std = 0.08	0.1914 (0.5213)	0.2764 (0.3243)	**0.1674** (0.9396)

by our discussion in section 1.2 and partially explained by the fact that the value of isotropic TV is less than that of anisotropic TV. In the following experiments, we investigate only the enhanced anisotropic TV model (1.7).

The second part illustrates the robustness of the enhanced TV model (1.7) with respect to noise. In this case, we still set α to 0.8 in the model (1.7), and we take measurements along 15 lines (corresponding to a 6.44% sampling rate) and use 6.5% MRI-desired samples. The Fourier measurements are perturbed by Gaussian noise with standard derivations ('std' for short) of 0.04, 0.06, and 0.08, respectively. The contamination process is implemented in MATLAB commands: For any image X with size $N \times N$, we first compute its Fourier measurements by the fast Fourier transform, i.e. `F = fft2(X)/N`. Then we perturb F by `F = F+1/sqrt(2)*(std*randn(size(F))+std*1i*randn(size(F)))`. The relative errors and SSIM values listed in table 2 show that the enhanced TV model (1.7) is the most robust one. In particular, in terms of SSIM values, the enhanced TV model (1.7) produces much better reconstruction quality, and the superiority is more apparent when the level of noise increases. These results assert the theoretical result in section 3.3 that the enhanced TV model (1.7) has a tighter reconstruction error bound than the TV model (1.2) and the $TV_a - TV_i$ model in [39] when the level of noise is relatively large.
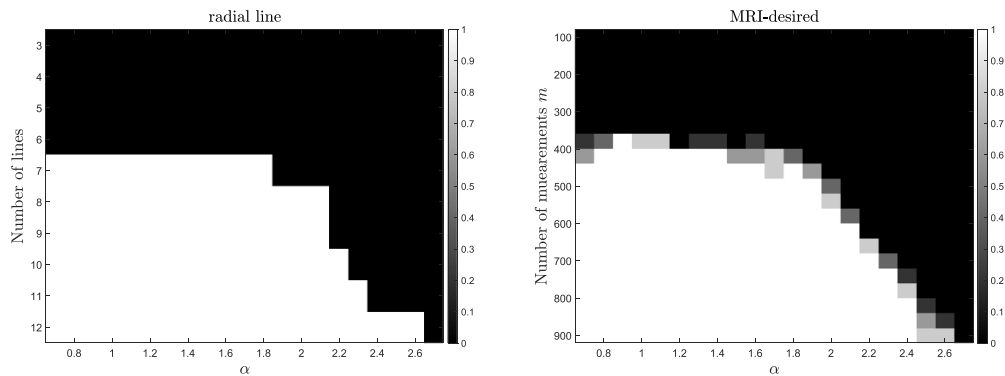
Figure 6. Phase transitions with respect to *m* and α.

The third part focuses on the phase transition of reconstruction success rates. A reconstruction is considered *successful* if the relative error of the reconstructed image is less than 10^{-3}. We consider the Shepp–Logan phantom with size 64×64 in this part. We choose α among $\{0.7, 0.8, \ldots, 2.7\}$ for the enhanced TV model (1.7). We choose the number of measurements *m* from 3 to 12 radial lines for radial sampling and among $\{100, 140, 180, \ldots, 900\}$ for MRI-desired sampling. For each case, we test five times and report the success rate. According to theorem 3.3, stable reconstruction can be achieved if samples are enough in the sense of (3.7) and the model parameter α is bounded in the sense of (3.16). The results in figure 6 assert that a successful reconstruction via the enhanced TV model (1.7) requires relatively sufficient samples and a reasonably bounded parameter α, thus validating results in theorem 3.3.

Example #2: Synthetic images. Example #1 shows the superiority of the enhanced TV model (1.7) for Shepp–Logan phantom with limited samples. The purpose of this study is to further assert this superiority. We consider the radial line sampling and validate this superiority by testing three synthetic images: Shape, Circle, and USC Mosaic. We also fix $\alpha = 0.8$ in the enhanced TV model (1.7). When the number of measurements is limited enough, all three models fails to generate good reconstructions. Bearing in mind that the criteria of the limitation on the amount of measurements are different for three models, we now show some cases that the reconstruction via the enhanced TV model (1.7) is particularly good while those via the TV model (1.2) and the $\text{TV}_a - \text{TV}_i$ model in [39] may fail. The reconstruction results are displayed in figure 7, and the relative errors and SSIM values are reported in table 3. From both figure 7 and table 3, the reconstruction of the enhanced TV model (1.7) is significantly better than the other two models.

We also take this example to test how the inner iterations can affect the overall performance of the algorithms under comparison. The algorithm presented in appendix C adopts DCA as the outer iteration and uses the alternating direction method of multiplier (ADMM) to solve each DCA subproblem. When the maximum number of inner ADMM iterations is increased from 1000 to 2000, the numerical results are reported in the fifth column of figure 7, labeled as 'Enhanced TV-2000'. We see that even if the enhanced TV model (1.7) with at most 1000 inner iterations is good enough to generate a satisfactory reconstruction, e.g. for Circle and USC Mosaic, increasing the number of inner iterations can further reduce the relative errors
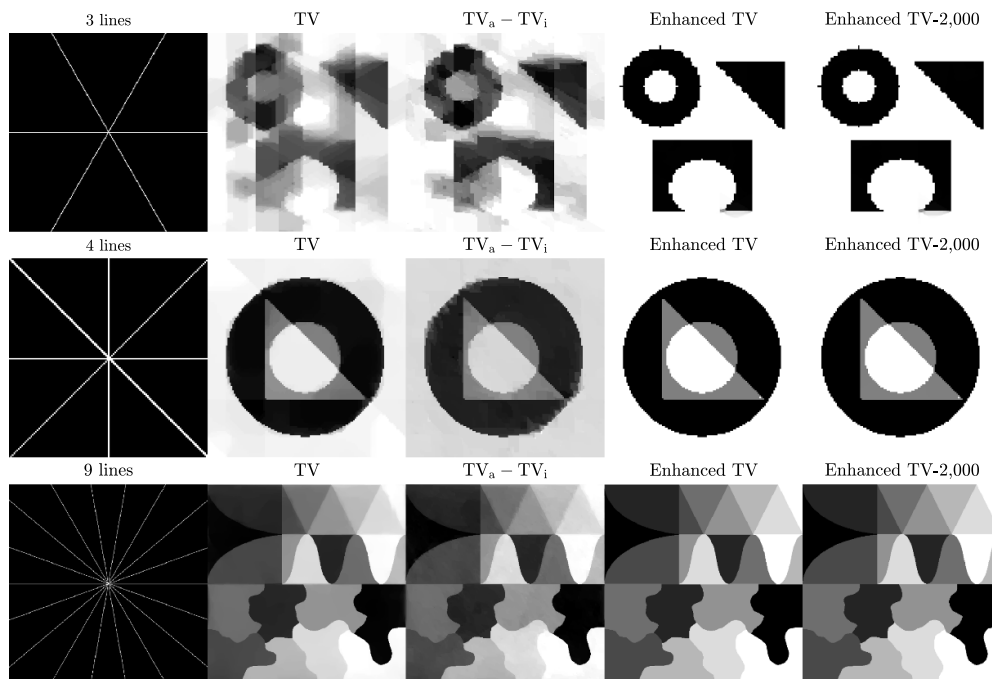
Figure 7. Shape, Circle, and USC Mosaic: comparison of three models with limited measurements.

Table 3. Relative errors and SSIM values of the reconstructed images in figure 7.

	TV	$TV_a - TV_i$	Enhanced TV	Enhanced TV-2000
Shape (1.29%)	0.3094 (0.5466)	0.2503 (0.5458)	**0.0266** (0.9932)	0.0261 (0.9937)
Circle (3.86%)	0.0394 (0.9705)	0.0498 (0.9430)	$\mathbf{7.411 \times 10^{-8}}$ (1.0000)	6.815×10^{-13} (1.0000)
USC Mosaic (1.95%)	0.0405 (0.9032)	0.0439 (0.9024)	$\mathbf{8.013 \times 10^{-5}}$ (1.0000)	4.206×10^{-7} (1.0000)

by up to several orders of magnitude. This observation provides a simple recipe for higher-accuracy reconstruction.

Example #3: Natural images. We further validate the superiority of the enhanced TV model (1.7) by testing it on two natural images: Peppers and Clock. We set α to 1 in the enhanced TV model (1.7) for both images and display the reconstruction results from 9.16% MRI-desired samples in figure 8. We also report the relative errors in the Frobenius sense and SSIM values for each reconstruction from MRI-desired samples of rates 9.16%, 13.7%, 18.3%, and 22.9% in table 4.

However, it is worth noting that the enhanced TV model (1.7) may not perform as effectively for natural images as it does for the images in Examples #1 and #2 due to the more
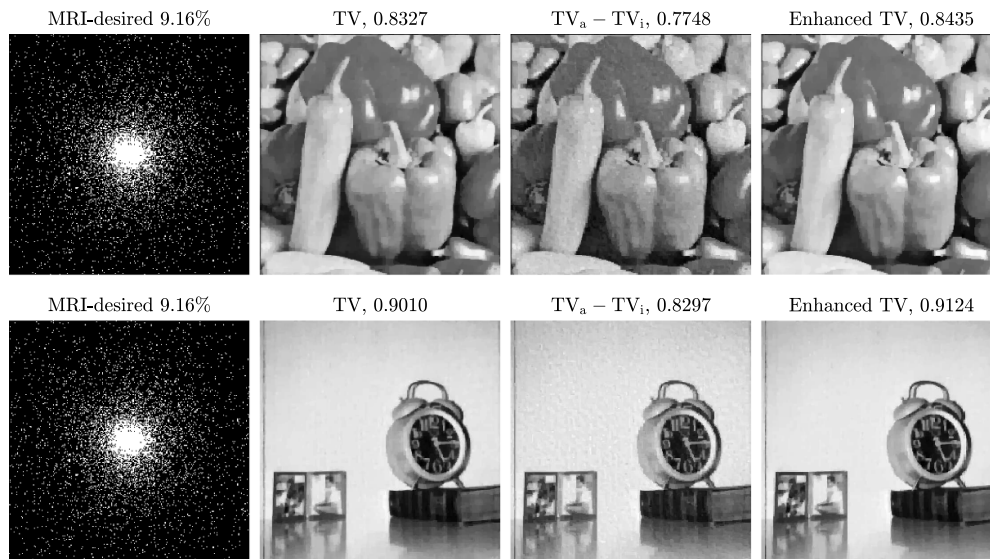
MRI-desired 9.16% | TV, 0.8327 | TV$_a$ − TV$_i$, 0.7748 | Enhanced TV, 0.8435

MRI-desired 9.16% | TV, 0.9010 | TV$_a$ − TV$_i$, 0.8297 | Enhanced TV, 0.9124

Figure 8. Peppers and Clock: comparison of three models with the MRI-desired sampling. SSIM values are also reported in the titles of each reconstruction.

Table 4. Relative errors and SSIM values of reconstructions of two natural images with various sampling rates.

	TV	TV$_a$ − TV$_i$	Enhanced TV
Peppers (9.16%)	0.0771 (0.8327)	0.0823 (0.7748)	**0.0718** (0.8435)
Peppers (13.73%)	0.0597 (0.8793)	0.0624 (0.8409)	**0.0536** (0.8908)
Peppers (18.31%)	0.0447 (0.9139)	0.0498 (0.8800)	**0.0414** (0.9208)
Peppers (22.89%)	0.0388 (0.9292)	0.0424 (0.9035)	**0.0351** (0.9358)
Clock (9.16%)	0.0404 (0.9010)	0.0440 (0.8297)	**0.0379** (0.9124)
Clock (13.73%)	0.0288 (0.9356)	0.0319 (0.8884)	**0.0272** (0.9421)
Clock (18.31%)	0.0213 (0.9563)	0.0246 (0.9218)	**0.0203** (0.9592)
Clock (22.89%)	0.0182 (0.9647)	0.0205 (0.9393)	**0.0169** (0.9674)

complicated (non-piecewise-constant) edges in natural images. Nonetheless, this observation is not surprising as the enhanced TV model (1.7) is a generalization of the TV model (1.2), which performs better for piecewise-constant images than natural images. The enhanced TV model (1.7) retains the main feature of the TV regularization while also reduces the loss of contrast.

Example #4: Medical images. Finally, we apply the enhanced TV model (1.7) to two medical images: Spine and Brain. We again set α to 1 and use 15.3% MRI-desired samples for the reconstruction of Spine and 9.16% for Brain. The reconstructed images are displayed in figure 9, and it is evident that that the enhanced TV model (1.7) produces better reconstructions compared to the other models. We also test more sampling rates and report the SSIM values of reconstructions with each rate in figure 10. We observe that the superiority of the enhanced TV model (1.7) is more apparent when the sampling rate is relatively low. Therefore, the enhanced TV model (1.7) is preferred when measurements are limited. Similar to Example
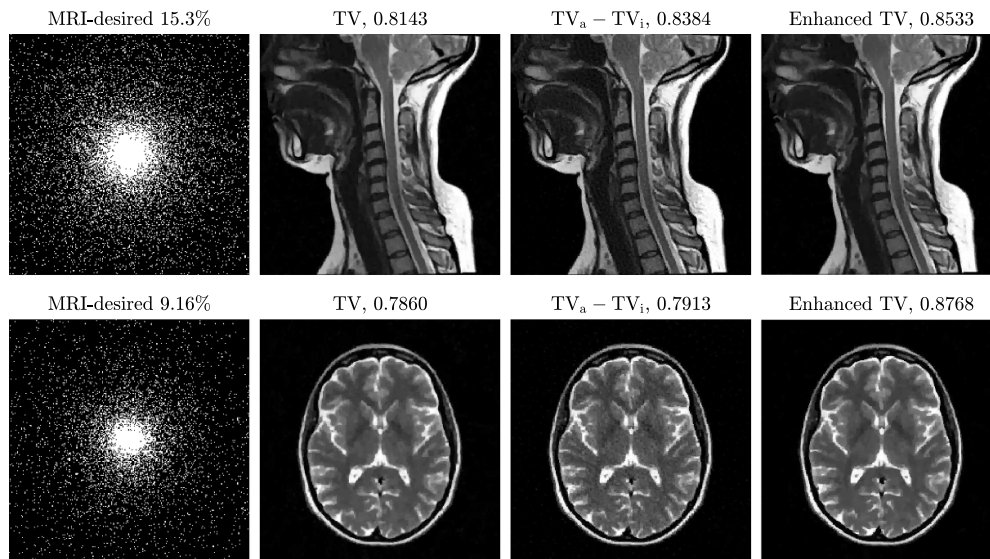
Figure 9. Spine and Brain: comparison of three models on medical images with the MRI-desired sampling. SSIM values are also reported in the titles of each reconstruction.
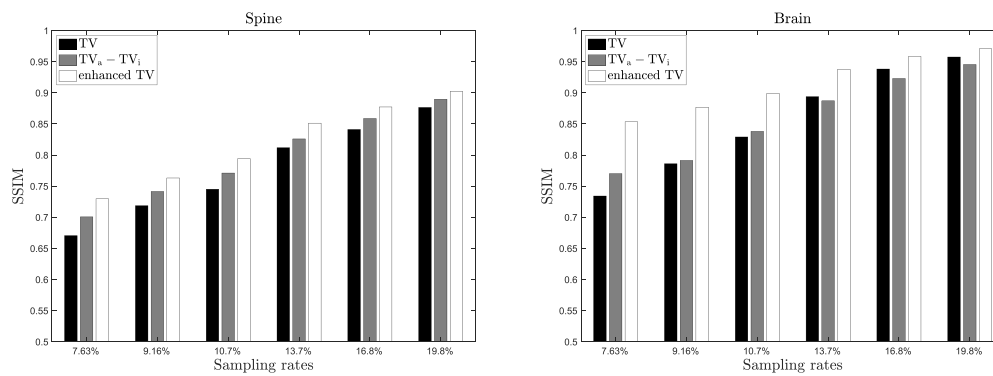

Figure 10. Spine and Brain: SSIM values of reconstructions with various sampling rates.

#3, the enhanced TV model (1.7) performs less effectively for Example #4 than Examples #1 and #2 due to the non-piecewise-constant edges of these medical images.

6. Conclusions

We focused on enhancing the canonical constrained TV minimization model for image reconstruction by the spingback regularization in our previous work [4]. The enhanced TV model improves the original TV model by adding a backward diffusion process to further reduce the loss of contrast. The reconstruction guarantees of the enhanced TV model (1.7) for non-adaptive subsampled linear RIP and variable-density subsampled Fourier measurements were theoretically established. For non-adaptive linear RIP measurements, the RIP level δ requirement was relaxed from $\delta < 1/3$ (which was derived for the TV model (1.2) in [47]) to

$\delta < 0.6$. The reconstruction error bounds estimated in theorems 3.1 and 3.2 also imply reasonable reconstruction error estimations for the TV model (1.2) when $\delta \to 0.6$. In contrast, the bounds derived in [47] for the TV model (1.2) tend to be infinity as $\delta \to 0.6$. For variable-density sampled Fourier measurements, the required minimum number of measurements of the enhanced TV model (1.7) was shown to be around 30.86% of that established in [36] for the TV model (1.2). This improvement is due to the relaxation of the requirement on δ.

It is worth noting that we only consider the anisotropic TV, and proofs of the main theoretical results can be easily extended to the isotropic TV case. In addition, our results can also be generalized in several other ways. For example, one can consider other sampling strategies, such as those in [1, 51], for Fourier samples as considered in theorem 3.3. For the guarantees analysis with Fourier measurements, noise is measured by the weighted ℓ_2-norm (see (3.17)). One can consider some other norms to measure noise, such as those in [1, 51]. Our theoretical results for two-dimensional images can also be extended to higher dimensional signals, as considered in [1, 46]. Furthermore, it seems promising to apply the enhanced TV model (1.7) to other problems such as image in painting and super-resolution problems, combining the enhanced TV regularization (1.6) with other data fidelity terms to model some problems such as image segmentation and motion estimation, and using the enhanced TV regularization (1.6) in combination with other widely-used convex and/or non-convex regularizers to model various more challenging image processing problems.

Data availability statement

All data that support the findings of this study are included within the article (and any supplementary files).

Acknowledgment

Appendix A. The enhanced TV model (1.7) in a continuum setting

Let $u : \Omega \to \mathbb{R}$ be an image, where the image domain Ω is a bounded and open subset of $\mathbb{R}^2$. The TV denoising model in [55] for a noisy image $u_0 : \Omega \to \mathbb{R}$ is formulated as

$$\min_u \ \mathcal{E}_{\mathrm{TV}}(u) := \int_\Omega |\nabla u| \mathrm{d}x + \frac{\mu}{2} \int_\Omega (u(x) - u_0(x))^2 \mathrm{d}x, \qquad (A.1)$$

where $x = (x_1, x_2) \in \Omega$, $|\nabla u| = \sqrt{(\partial_{x_1} u)^2 + (\partial_{x_2} u)^2}$, and $\mu > 0$ balances the TV term and the data fidelity term. Note that the isotropic TV proposed in [55] is used in the model (A.1). Though the anisotropic TV defined in [24] is used in the enhanced TV regularization (1.6), the main purpose of this appendix is to explain how the TV is enhanced in the sense of (1.6). Thus, we adopt the model (A.1) for simplicity. We refer the reader to [44] for the anisotropic TV flow. More specifically, the enhanced (isotropic) TV denoising model in a continuum setting can be written as

$$\min_u \ \mathcal{E}_{\mathrm{ETV}}(u) := \int_\Omega |\nabla u| \mathrm{d}x - \frac{\alpha}{2} \int_\Omega |\nabla u|^2 \mathrm{d}x + \frac{\mu}{2} \int_\Omega (u(x) - u_0(x))^2 \mathrm{d}x. \quad (A.2)$$

Then, by computing the first-order variation of the functional, the E–L equation associated with the energy functional $\mathcal{E}_{\mathrm{ETV}}(u)$ in the distributional sense is

$$0 = -\nabla \cdot \left[\frac{\nabla u}{|\nabla u|} \right] + \alpha \Delta u + \mu(u - u_0) \quad \text{with} \quad \left. \frac{\partial u}{\partial \mathbf{n}} \right|_{\partial \Omega} = 0, \tag{A.3}$$

where $\mathbf{n}$ denotes the outer normal derivative along the boundary $\partial \Omega$ of Ω.

Alternatively, as [55], we could use the *gradient descent marching with artificial time t*. That is, the solution procedure of the E–L equation (A.3) uses a parabolic equation with time t as an evolution parameter. This means, for $u : \Omega \times [0, T] \to \mathbb{R}$, we solve

$$u_t = -\frac{\partial \mathcal{E}_{\mathrm{ETV}}}{\partial u} = \nabla \cdot \left[\frac{\nabla u}{|\nabla u|} \right] - \alpha \Delta u - \mu(u - u_0) \quad \text{for } t > 0, \, x \in \Omega, \tag{A.4}$$

with a given initial condition $u(x, 0)$ and the boundary condition $\frac{\partial u}{\partial \mathbf{n}}|_{\partial \Omega} = 0$. Note that there is a backward diffusion term $-\alpha \Delta u$ in the evolution equation (A.4). Thus, as t increases, we approach a denoised and deblurred version of the image if the blur is assumed to follow such a diffusion process.

If the energy functional $\mathcal{E}_{\mathrm{ETV}}(u)$ has a minimum, then the minimizer must satisfy the E–L equation (A.4). Certainly, the existence of the minimizer of $\mathcal{E}_{\mathrm{ETV}}$ is unknown for an arbitrary α. On the other hand, with $\alpha < \mu \inf_{x \in \Omega} \frac{|u(x)|^2}{|\nabla u(x)|^2}$, the Lagrangian

$$\mathcal{L}_{\mathrm{ETV}}(\nabla u, u, x) := |\nabla u| - \frac{\alpha}{2}|\nabla u|^2 + \frac{\mu}{2}(u(x) - u_0(x))^2$$

is bounded below by $|\nabla u(x)| + \frac{\mu - \alpha}{2}|u(x)|^2 - \mu u(x)u_0(x) + |u_0(x)|^2$, which is a convex function with respect to variables ∇u and u. Hence, $\mathcal{E}_{\mathrm{ETV}}$ is bounded below, and any stationary point u^* of $\mathcal{E}_{\mathrm{ETV}}$ (including global and local minimizers) must be finite and satisfy the corresponding EL equation (A.4) involving the backward diffusion term. This requirement on α explains the rationale of the assumption on the upper bound of α in theorems 3.1–3.3 (e.g. $\alpha \leqslant \frac{\sqrt{48 s \log(N)}}{K_2 \|\nabla X^{\mathrm{opt}}\|_2}$ in theorems 3.2 and 3.3).

Appendix B. Implementation details for reproducing figure 1

For denoising, let the noisy image be $y = \bar{X} + e \in \mathbb{C}^{N \times N}$. The denoising model using the enhanced TV regularization (1.6) is formulated as

$$\min_{X \in \mathbb{C}^{N \times N}} \|\nabla X\|_1 - \frac{\alpha}{2}\|\nabla X\|_2^2 + \frac{\mu}{2}\|y - X\|_2^2, \tag{B.1}$$

where $\mu > 0$ is a parameter balancing the enhanced TV regularization term and the data fidelity term. Note that the model (B.1) is the discretization of the model (A.2). The model (B.1) can be solved by the DCA in [59, 60], and its subproblems can be solved by the splitting Bregman iteration in [32]. We summarize the resulting algorithm as algorithm 1 below, in which MaxDCA denotes the maximum number of the DCA iterations and MaxBreg denotes is the maximum number of the Bregman iterations.

Algorithm 1. Solving the unconstrained denoising model (B.1).

Input: Define $X^0 = 0$, $z = 0$, $k = 0$, $d_x = d_y = 0$, MaxDCA and MaxBreg
1 while $k <$ MaxDCA **do**
2 $\quad b_x = b_y = 0$, $p = 0$;
3 $\quad$ **while** $p <$ MaxBreg **do**
4 $\quad\quad u = \left(\mu + \beta\nabla^{\mathrm{T}}\nabla\right)^{-1}\left(\mu y + \beta D_x^{\mathrm{T}}(d_x - b_x) + \beta D_y^{\mathrm{T}}(d_y - b_y)\right)$;
5 $\quad\quad d_x = \mathrm{shrink}\left(D_x u + b_x + \alpha D_x X^k/\beta, 1/\beta\right)$;
6 $\quad\quad d_y = \mathrm{shrink}\left(D_y u + b_y + \alpha D_y X^k/\beta, 1/\beta\right)$;
7 $\quad\quad b_x = b_x + D_x u - d_x$;
8 $\quad\quad b_y = b_y + D_y u - d_y$;
9 $\quad\quad p \leftarrow p + 1$;
10 $\quad$ **end**
11 $\quad X^k = u$;
12 $\quad k \leftarrow k + 1$;
13 end

To reproduce figure 1, we test the noisy *Strip* image (displayed in figure 1) with size 128×128. The parameters for algorithm 1 are set as $\alpha = 1.2$, $\mu = 0.8$, $\beta = 1$, MaxDCA $= 10$, and MaxBreg $= 1000$. We contaminate the test image by adding random values onto each pixel from a normal distribution with mean 0 and standard deviation 0.6, without normalizing all pixel intensities such that they are in the range of $[0, 1]$. We adopt the same parameters for the splitting Bregman iteration for solving the TV denoising model except that the number of the splitting Bregman iterations is set as 10 000.

Appendix C. DCA for the enhanced TV model (1.7)

We apply the mentioned DCA in [59, 60] to solve the enhanced TV model (1.7). We denote by $D_x X$ and $D_y X$ the horizontal and vertical components of ∇X, respectively, where D_x and D_y can be deemed as two operators. The DCA replaces the second component $\frac{\alpha}{2}\|\nabla X\|_2^2$ of the enhanced TV regularization term (1.6) by a linear majorant $\langle X - X^k, \xi^k \rangle$, where $\xi^k \in \partial\left(\frac{\alpha}{2}\|\nabla X\|_2^2\right) = \{\alpha\nabla^{\mathrm{T}}\nabla X^k\}$, and then solves the resulting convex optimization problem to generate the iterate X^{k+1}. Ignoring the constant term $\langle X^k, \xi^k \rangle$ in the objective function, the iterative scheme of the DCA reads as

$$X^{k+1} \in \arg\min_{X \in \mathbb{C}^{N \times N}} \left\{ \|D_x X\|_1 + \|D_y X\|_1 - \alpha\langle D_x X, D_x X^k \rangle - \alpha\langle D_y X, D_y X^k \rangle \right.$$
$$\left. \text{s.t. } \|\mathcal{M}X - y\|_2 \leqslant \tau \right\}. \tag{C.1}$$

Convergence of the DCA (C.1) can be found in, e.g. [4, 59, 60]. Recall that a convex function $F : \mathbb{R}^d \to \mathbb{R}$ is said to be *ρ-strongly convex* if $F(x) - \frac{\rho}{2}\|x\|_2^2$ is convex on $\mathbb{R}^d$. A simple but critical fact ensuring the convergence is that the component $\frac{\alpha}{2}\|\nabla X\|_2^2$ is strongly convex either if X is mean-zero or if X contains zero-valued pixels (cf the classical Sobolev inequality (4.5) and equation (4.7)).

To solve (C.1), we suggest using the benchmark ADMMs in [31]. Clearly, X^{k+1} is also a solution to the reformulated problem

$$\begin{aligned} \min \quad & \|d_x\|_1 + \|d_y\|_1 - \alpha\langle d_x, D_x X^k \rangle - \alpha\langle d_y, D_y X^k \rangle, \\ \text{s.t.} \quad & \mathcal{M}X - y - z = 0, \\ & z \in \mathcal{B}(0, \tau) := \{x \in \mathbb{R}^m : \|x\|_2 \leqslant \tau\}, \\ & D_x X = d_x, \quad D_y X = d_y. \end{aligned} \tag{C.2}$$

Introducing three Lagrange multipliers λ, b_x, and b_y, we write the augmented Lagrangian function of (C.2) as

$$
\begin{aligned}
\mathcal{L}_{\beta,\mu}(X, d_x, d_y, z, b_x, b_y, \lambda) := & \|d_x\|_1 + \|d_y\|_1 - \alpha\langle d_x, D_x X^k\rangle - \alpha\langle d_y, D_y X^k\rangle \\
& + \frac{\mu}{2}\|z - (\mathcal{M}X - y) - \lambda\|_2^2 + \frac{\beta}{2}\|d_x - D_x X - b_x\|_2^2 \\
& + \frac{\beta}{2}\|d_y - D_y X - b_y\|_2^2,
\end{aligned}
$$

where $\mu, \beta > 0$ are penalty parameters. Implementations of the ADMM to (C.1) are included as algorithm 1 below, in which MaxDCA denotes the maximum number of the DCA iterations, MaxADMM is the maximum number of the ADMM iterations for (C.2) with a given X^k, and 'tol' is the tolerance for the DCA iterations. If the TV term $\|X\|_{\mathrm{TV}_a} = \|\nabla X\|_1$ is replaced by the isotropic version, then $D_x X$ and $D_x X$ in (C.1) or d_x and d_y in (C.2) do not decouple while we can still update d_x and d_y in a closed-form manner. Like the extension from the anisotropic TV to the isotropic one in [32], to solve the enhanced isotropic TV model, we merely need to replace lines 5 and 6 in algorithm 2 with

- $s = \sqrt{|D_x u + b_x + \alpha D_x X^k/\beta|.^2 + |D_y u + b_y + \alpha D_y X^k/\beta|.^2}$;
- $d_x = \max(s - 1/\beta, 0).*(D_x u + b_x + \alpha D_x X^k/\beta)./s$;
- $d_y = \max(s - 1/\beta, 0).*(D_y u + b_y + \alpha D_y X^k/\beta)./s$;

where the point '.' before operations denotes entry-wise operations.

Algorithm 2. DCA for the enhanced TV model (1.7).

Input: Define $X^0 = 0$, $z = 0$, $k = 0$, $d_x = d_y = 0$, MaxDCA, MaxADMM, and tol
1 **while** $k <$ MaxDCA and $\|X^k - X^{k-1}\|_2 >$ tol **do**
2 $\quad | \quad b_x = b_y = 0, p = 0$;
3 $\quad |$ **while** $p <$ MaxADMM **do**
4 $\quad | \quad | \quad u = \left(\mu\mathcal{M}^*\mathcal{M} + \beta\nabla^{\mathrm{T}}\nabla\right)^{-1}\left(\mu\mathcal{M}^*(y - z - \lambda) + \beta D_x^{\mathrm{T}}(d_x - b_x) + \beta D_y^{\mathrm{T}}(d_y - b_y)\right)$;
5 $\quad | \quad | \quad d_x = \mathrm{shrink}\left(D_x u + b_x + \alpha D_x X^k/\beta, 1/\beta\right)$;
6 $\quad | \quad | \quad d_y = \mathrm{shrink}\left(D_y u + b_y + \alpha D_y X^k/\beta, 1/\beta\right)$;
7 $\quad | \quad | \quad z = \mathcal{P}_{\mathcal{B}(0,\tau)}(\mathcal{M}u - y + \lambda)$;
8 $\quad | \quad | \quad b_x = b_x + D_x u - d_x$;
9 $\quad | \quad | \quad b_y = b_y + D_y u - d_y$;
10 $\quad | \quad | \quad \lambda = \lambda + (\mathcal{M}u - y) - z$;
11 $\quad | \quad | \quad p \leftarrow p + 1$;
12 $\quad |$ **end**
13 $\quad | \quad X^k = u$;
14 $\quad | \quad k \leftarrow k + 1$;
15 **end**

In our numerical experiments, to implement algorithm 2, we set $\mu = 10^3$, $\beta = 10$, MaxDCA $= 15$, tol $= 10^{-10}$ (for noise-free measurements) or 10^{-3} (for noisy measurements), and MaxADMM $= 1000$. For the $\mathrm{TV}_a - \mathrm{TV}_i$ model in [39], we use the same penalty parameters and stopping criterion for running the DCA; and for the split Bregman method in solving the DCA subproblem, we set the maximum numbers of outer and inner iterations as 50 and 20, respectively. The parameters for Bregman iterations were suggested in [39], and they coincide with the maximum number of the inner ADMM iterations in algorithm 2, as $50 \times 20 = 1000$. For the TV model (1.2), we adopt the same penalty parameters and tolerance for outer iterations.

We set the maximal numbers of outer and inner iterations to be 50 and 200, respectively; both numbers were suggested in [39].

ORCID iDs

Hao-Ning Wu ⬡ https://orcid.org/0000-0002-5716-9427
Xiaoming Yuan ⬡ https://orcid.org/0000-0002-6900-6983

References

[1] Adcock B, Dexter N and Xu Q 2021 Improved recovery guarantees and sampling strategies for TV minimization in compressive imaging *SIAM J. Imaging Sci.* **14** 1149–83
[2] Adcock B, Hansen A C, Poon C and Roman B 2017 Breaking the coherence barrier: a new theory for compressed sensing *Forum Math. Sigma* **5** e4
[3] Alvarez L and Mazorra L 1994 Signal and image restoration using shock filters and anisotropic diffusion *SIAM J. Numer. Anal.* **31** 590–605
[4] An C, Wu H-N and Yuan X 2022 The springback penalty for robust signal recovery *Appl. Comput. Harmon. Anal.* **61** 319–46
[5] Benning M, Brune C, Burger M and Müller J 2013 Higher-order TV methods—enhancement via Bregman iteration *J. Sci. Comput.* **54** 269–310
[6] Bi N and Tang W-S 2022 A necessary and sufficient condition for sparse vector recovery via $\ell_1 - \ell_2$ minimization *Appl. Comput. Harmon. Anal.* **56** 337–50
[7] Blomgren P, Chan T F, Mulet P and Wong C-K 1997 Total variation image restoration: numerical methods and extensions *Proc. Int. Conf. on Image Processing* (IEEE) pp 384–7
[8] Bredies K, Kunisch K and Pock T 2010 Total generalized variation *SIAM J. Imaging Sci.* **3** 492–526
[9] Cai J-F and Xu W 2015 Guarantees of total variation minimization for signal recovery *Inf. Inference J. IMA* **4** 328–53
[10] Candès E J, Romberg J and Tao T 2006 Robust uncertainty principles: exact signal reconstruction from highly incomplete frequency information *IEEE Trans. Inf. Theory* **52** 489–509
[11] Candès E J and Tao T 2005 Decoding by linear programming *IEEE Trans. Inf. Theory* **51** 4203–15
[12] Candès E J and Tao T 2006 Near-optimal signal recovery from random projections: universal encoding strategies? *IEEE Trans. Inf. Theory* **52** 5406–25
[13] Chambolle A 2004 An algorithm for total variation minimization and applications *J. Math. Imaging Vis.* **20** 89–97
[14] Chambolle A 2005 Total variation minimization and a class of binary MRF models *Int. Workshop on Energy Minimization Methods in Computer Vision and Pattern Recognition* (Berlin: Springer) pp 136–52
[15] Chambolle A, Caselles V, Cremers D, Novaga M and Pock T 2010 An introduction to total variation for image analysis *Theoretical Foundations and Numerical Methods for Sparse Recovery* (Berlin: De Gruyter) pp 263–340
[16] Chambolle A and Lions P-L 1997 Image recovery via total variation minimization and related problems *Numer. Math.* **76** 167–88
[17] Chambolle A and Pock T 2016 An introduction to continuous optimization for imaging *Acta Numer.* **25** 161–319
[18] Chambolle A and Pock T 2021 Approximating the total variation with finite differences or finite elements *Handbook of Numerical Analysis* vol 22 (Amsterdam: Elsevier) pp 383–417
[19] Chambolle A and Pock T 2021 Learning consistent discretizations of the total variation *SIAM J. Imaging Sci.* **14** 778–813
[20] Chan T F, Marquina A and Mulet P 2000 High-order total variation-based image restoration *SIAM J. Sci. Comput.* **22** 503–16
[21] Chartrand R 2007 Exact reconstruction of sparse signals via nonconvex minimization *IEEE Signal Process. Lett.* **14** 707–10
[22] Conway J H and Guy R K 1996 *The Book of Numbers* (New York: Copernicus) (https://doi.org/10.1007/978-1-4612-4072-3)
[23] Donoho D L 2006 Compressed sensing *IEEE Trans. Inf. Theory* **52** 1289–306

[24] Esedoḡlu S and Osher S 2004 Decomposition of images by the anisotropic Rudin–Osher–Fatemi model *Commun. Pure Appl. Math.* **57** 1609–26

[25] Fan J and Li R 2001 Variable selection via nonconcave penalized likelihood and its oracle properties *J. Am. Stat. Assoc.* **96** 1348–60

[26] Fannjiang A C, Strohmer T and Yan P 2010 Compressed remote sensing of sparse objects *SIAM J. Imaging Sci.* **3** 595–618

[27] Foucart S and Lai M-J 2009 Sparsest solutions of underdetermined linear systems via ℓ_q-minimization for $0 < q \leqslant 1$ *Appl. Comput. Harmon. Anal.* **26** 395–407

[28] Galdran A, Vazquez-Corral J, Pardo D and Bertalmio M 2015 Enhanced variational image dehazing *SIAM J. Imaging Sci.* **8** 1519–46

[29] Ge H and Li P 2021 The Dantzig selector: recovery of signal via $\ell_1 - \alpha\ell_2$ minimization *Inverse Problems* **38** 015006

[30] Gilboa G, Sochen N and Zeevi Y Y 2002 Forward-and-backward diffusion processes for adaptive image enhancement and denoising *IEEE Trans. Image Process.* **11** 689–703

[31] Glowinski R and Marrocco A 1975 Sur l'approximation, par éléments finis d'ordre un, et la résolution, par pénalisation-dualité, d'une classe de problèmes de Dirichlet non linéaires *Rev. Fr. Autom. Inform. Rech. Oper.* **9** 41–76

[32] Goldstein T and Osher S 2009 The split Bregman method for L1-regularized problems *SIAM J. Imaging Sci.* **2** 323–43

[33] Huo L, Chen W, Ge H and Ng M K 2022 Stable image reconstruction using transformed total variation minimization *SIAM J. Imaging Sci.* **15** 1104–39

[34] Krahmer F, Kruschel C and Sandbichler M 2017 Total variation minimization in compressed sensing *Compressed Sensing and its Applications* (Cham: Birkhäuser/Springer) pp 333–58

[35] Krahmer F and Ward R 2011 New and improved Johnson–Lindenstrauss embeddings via the restricted isometry property *SIAM J. Math. Anal.* **43** 1269–81

[36] Krahmer F and Ward R 2014 Stable and robust sampling strategies for compressive imaging *IEEE Trans. Image Process.* **23** 612–22

[37] Li P, Chen W, Ge H and Ng M K-P 2020 $\ell_1 - \alpha\ell_2$ minimization methods for signal and image reconstruction with impulsive noise removal *Inverse Problems* **36** 055009

[38] Lou Y, Yin P, He Q and Xin J 2015 Computing sparse representation in a highly coherent dictionary based on difference of l_1 and l_2 *J. Sci. Comput.* **64** 178–96

[39] Lou Y, Zeng T, Osher S and Xin J 2015 A weighted difference of anisotropic and isotropic total variation model for image processing *SIAM J. Imaging Sci.* **8** 1798–823

[40] Lustig M, Donoho D and Pauly J M 2007 Sparse MRI: the application of compressed sensing for rapid MR imaging *Magn. Reson. Med.* **58** 1182–95

[41] Lustig M, Donoho D L, Santos J M and Pauly J M 2008 Compressed sensing MRI *IEEE Signal Process. Mag.* **25** 72–82

[42] Ma T-H, Lou Y and Huang T-Z 2017 Truncated ℓ_{1-2} models for sparse recovery and rank minimization *SIAM J. Imaging Sci.* **10** 1346–80

[43] Mendelson S, Pajor A and Tomczak-Jaegermann N 2007 Reconstruction and subgaussian operators in asymptotic geometric analysis *Geom. Funct. Anal.* **17** 1248–82

[44] Moll J S 2005 The anisotropic total variation flow *Math. Ann.* **332** 177–218

[45] Möllenhoff T, Strekalovskiy E, Moeller M and Cremers D 2015 The primal-dual hybrid gradient method for semiconvex splittings *SIAM J. Imaging Sci.* **8** 827–57

[46] Needell D and Ward R 2013 Near-optimal compressed sensing guarantees for total variation minimization *IEEE Trans. Image Process.* **22** 3941–9

[47] Needell D and Ward R 2013 Stable image reconstruction using total variation minimization *SIAM J. Imaging Sci.* **6** 1035–58

[48] Nikolova M 2015 Energy minimization methods *Handbook of Mathematical Methods in Imaging* (New York: Springer) pp 157–204

[49] Osher S and Rudin L I 1990 Feature-oriented image enhancement using shock filters *SIAM J. Numer. Anal.* **27** 919–40

[50] Pierre F, Aujol J-F, Bugeau A, Steidl G and Ta V-T 2017 Variational contrast enhancement of grayscale and RGB images *J. Math. Imaging Vis.* **57** 99–116

[51] Poon C 2015 On the role of total variation in compressed sensing *SIAM J. Imaging Sci.* **8** 682–720

[52] Rauhut H, Romberg J and Tropp J A 2012 Restricted isometries for partial random circulant matrices *Appl. Comput. Harmon. Anal.* **32** 242–54

[53] Rauhut H and Ward R 2012 Sparse Legendre expansions via ℓ_1-minimization *J. Approx. Theory* **164** 517–33

[54] Rudelson M and Vershynin R 2008 On sparse reconstruction from Fourier and Gaussian measurements *Commun. Pure Appl. Math.* **61** 1025–45

[55] Rudin L I, Osher S and Fatemi E 1992 Nonlinear total variation based noise removal algorithms *Physica* D **60** 259–68

[56] Setzer S and Steidl G 2008 Variational methods with higher-order derivatives in image processing *Approximation Theory XII: San Antonio 2007* (*Modern Methods in Mathematics*) (Brentwood, TN: Nashboro Press) pp 360–85

[57] Setzer S, Steidl G and Teuber T 2011 Infimal convolution regularizations with discrete ℓ_1-type functionals *Commun. Math. Sci.* **9** 797–827

[58] Strong D and Chan T F 2003 Edge-preserving and scale-dependent properties of total variation regularization *Inverse Problems* **19** S165

[59] Tao P D and An L T H 1997 Convex analysis approach to DC programming: theory, algorithms and applications *Acta Math. Vietnam.* **22** 289–355

[60] Tao P D and An L T H 1998 A DC optimization algorithm for solving the trust-region subproblem *SIAM J. Optim.* **8** 476–505

[61] Tikhonov A N and Arsenin V Y 1977 *Solutions of ill-Posed Problems* (Washington, DC: Wiley) (Translated from the Russian, Preface by translation editor Fritz John)

[62] Welk M, Gilboa G and Weickert J 2009 Theoretical foundations for discrete forward-and-backward diffusion filtering *Int. Conf. on Scale Space and Variational Methods in Computer Vision* (Springer) pp 527–38

[63] Welk M, Steidl G and Weickert J 2008 Locally analytic schemes: a link between diffusion filtering and wavelet shrinkage *Appl. Comput. Harmon. Anal.* **24** 195–224

[64] Welk M, Theis D, Brox T and Weickert J 2005 PDE-based deconvolution with forward-backward diffusivities and diffusion tensors *Int. Conf. on Scale-Space Theories in Computer Vision* (Springer) pp 585–97

[65] Welk M, Weickert J and Galić I 2007 Theoretical foundations for spatially discrete 1-D shock filtering *Image Vis. Comput.* **25** 455–63

[66] Welk M, Weickert J and Gilboa G 2018 A discrete theory and efficient algorithms for forward-and-backward diffusion filtering *J. Math. Imaging Vis.* **60** 1399–426

[67] Wen J, Weng J, Tong C, Ren C and Zhou Z 2019 Sparse signal recovery with minimization of 1-norm minus 2-norm *IEEE Trans. Veh. Technol.* **68** 6847–54

[68] Yan L, Shin Y and Xiu D 2017 Sparse approximation using $\ell_1 - \ell_2$ minimization and its application to stochastic collocation *SIAM J. Sci. Comput.* **39** A229–54

[69] Yin P, Lou Y, He Q and Xin J 2015 Minimization of ℓ_{1-2} for compressed sensing *SIAM J. Sci. Comput.* **37** A536–63

[70] You J, Jiao Y, Lu X and Zeng T 2019 A nonconvex model with minimax concave penalty for image restoration *J. Sci. Comput.* **78** 1063–86

[71] Zhang C-H 2010 Nearly unbiased variable selection under minimax concave penalty *Ann. Stat.* **38** 894–942

[72] Zhang S and Xin J 2017 Minimization of transformed L_1 penalty: closed form representation and iterative thresholding algorithms *Commun. Math. Sci.* **15** 511–37

[73] Zhang S and Xin J 2018 Minimization of transformed L_1 penalty: theory, difference of convex function algorithm and robust application in compressed sensing *Math. Program.* **169** 307–36